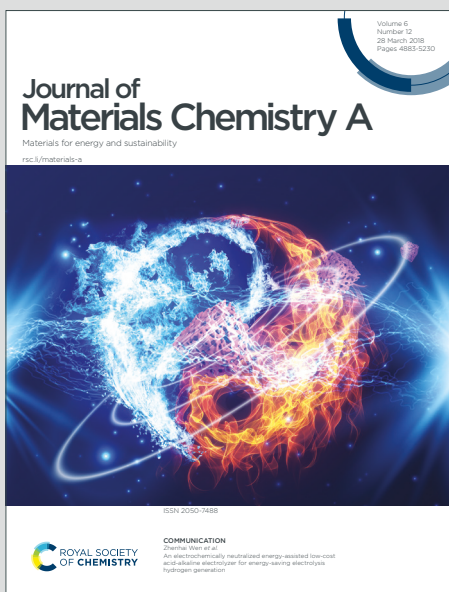


Journal of Materials Chemistry A

Materials for energy and sustainability

Accepted Manuscript

This article can be cited before page numbers have been issued, to do this please use: W. MacSwain, X. Hu, R. Wu, Z. Li, V. Vanshika, D. Ma, O. Chen and W. Zheng, *J. Mater. Chem. A*, 2026, DOI: 10.1039/D5TA08886K.



This is an Accepted Manuscript, which has been through the Royal Society of Chemistry peer review process and has been accepted for publication.

Accepted Manuscripts are published online shortly after acceptance, before technical editing, formatting and proof reading. Using this free service, authors can make their results available to the community, in citable form, before we publish the edited article. We will replace this Accepted Manuscript with the edited and formatted Advance Article as soon as it is available.

You can find more information about Accepted Manuscripts in the [Information for Authors](#).

Please note that technical editing may introduce minor changes to the text and/or graphics, which may alter content. The journal's standard [Terms & Conditions](#) and the [Ethical guidelines](#) still apply. In no event shall the Royal Society of Chemistry be held responsible for any errors or omissions in this Accepted Manuscript or any consequences arising from the use of any information it contains.

ARTICLE

Received 00th January 20xx,
Accepted 00th January 20xx

DOI: 10.1039/x0xx00000x

Noble-Metal-Free Metal Hydroxide Co-Catalyst Coupled Mn(II)-Doped CdS Nanorods with Bridged Charge Transport for Enhanced Photocatalytic Hydrogen Generation**Walker MacSwain,^b Xia Hu,^{†a} Rongzhen Wu,^c Zhi-Jun Li,^b Vanshika Vanshika,^b De-Kun Ma,^d Ou Chen,^c Weiwei Zheng^{b†}**

Clean and renewable energy from sunlight utilization offers significant opportunities for addressing on-going energy and environmental crises. In this work, Mn(II) doped 1-dimensional (1D) CdS nanorods (NRs) modified with metal hydroxides ($M(OH)_x$, $M = Ni^{2+}$, Co^{2+} , and Fe^{3+}) were synthesized as noble metal free photocatalysts for hydrogen generation from water splitting. The incorporation of Mn(II) dopants inside the CdS NRs with a longer lifetime ($\sim ms$) than that of the host CdS ($\sim ns$) leads to efficient charge separation and subsequent electron transfer, which is more efficient due to the longer lifetime Mn(II) dopants, to $M(OH)_x$ results in higher photocatalytic activity towards water splitting. Interestingly, $Ni(OH)_2$ has the highest efficiency towards photocatalysis under neutral conditions (2.1 fold increase), while the other $M(OH)_x$ ($M = Co^{2+}$ and Fe^{3+}) decorated NRs utilized higher pH values (>13, 2.9 and 2.2 fold increase, respectively) for increased photocatalysis. This can be understood through the changing stable phase in a potential/pH diagram (Pourbaix diagram); at higher pH values, the stable phase of $Ni(OH)_2$ is $Ni(OH)_3^-$ which has a Coulombic repulsive force lowering the ability of photogenerated electrons to transfer to the co-catalytic surface for photo-redox reactions. Enhanced charge transport from a small number of Mn(II) dopants ($\sim 0.9\%$ Mn dopants in a CdS NR) efficiently results in increased photocatalysis for the resulting Mn:CdS- $M(OH)_x$ NRs.

Introduction

The ongoing environmental and energy crises require clean, green energy solutions to alleviate issues stemming from improper renewable resource utilization. Quantum confined semiconductor nanocrystals (NCs), such as CdSe¹⁻³ and CdS⁴⁻⁶, are often utilized as photocatalysts due to having excellent optoelectronic properties including large absorption extinction coefficients in the visible range, size-tunable bandgaps, and shape-dependent charge polarizations across the unconfined axis/axes.⁶⁻⁹ Altering the morphology of a CdS-based semiconductor, to a 1D CdS nanorod (NR)¹⁰ (unconfined across 1 axis) or a 2D nanoplatelet (unconfined across 2 axes),¹¹ allows photogenerated electrons to travel, increasing the possibility of an exciton diffusing away from its localized hole pair leading to increased photocatalytic redox activity.¹² However, CdS, like many other semiconductor NCs, suffers from rapid charge recombination ($\sim ns$) which is both significantly slower than that of surface reactions ($\sim ms$ to s)^{9,13-15} and has therefore limited

charge carriers available to partake in photocatalytic redox reactions.

To overcome this limitation, co-catalysts have been added to CdS-based hybrid semiconductor nanostructures.⁶ The co-catalysts can provide electron transfer and/or energy transfer to Fermi energy level active sites for efficient surface redox reactions. Common co-catalyst utilization can either come as a semiconductor such as TiO_2 ¹⁶⁻¹⁸, ZnO ¹⁹⁻²¹, CeO_2 ^{22,23} etc., or as a metal such as Pt^{11,24,25} and Au^{17,26,27}, etc. Co-catalysts provide active sites that facilitate the migration and accumulation of photogenerated electrons and/or holes, thereby enhancing charge separation, prolonging the lifetime of charge-separated states, and promoting efficient surface redox reactions.^{24,28-31} The longer the photo-induced charge separation, the greater the likelihood of the charge carriers being utilized in photocatalytic redox reactions. Co-catalytic active sites also enhance stability as photocatalysis on the surface of CdS can result in photo-degradation and the formation of SO_4^{2-} on the surface of CdS which poisons the photocatalyst.³²⁻³⁴

While noble metals have often been reported for their excellent photocatalytic properties for hydrogen reduction, they are often extremely expensive which makes their widespread utilization significantly challenging. Therefore, significant efforts have been made to replace noble metals with low-cost alternatives, particularly earth abundant first row transition metals such as Ni, Co, and Fe.³⁵⁻⁴⁶ However, first row transition metals are fairly unstable in their metallic forms and often undergo oxidation state changes, such as Ni^{2+} to Ni^+ under

^a [†]School of Life and Environmental Sciences, Shaoxing University, Shaoxing, 312000, P. R. China **E-mail:** huxia1111@usx.edu.cn^b Department of Chemistry, Syracuse University, Syracuse 13244, New York, USA **E-mail:** wzhen104@syr.edu^c Department of Chemistry, Brown University, Providence, 02912, Rhode Island, USA^d Zhejiang Key Laboratory of Functional ionic membrane Materials and Technology for Hydrogen Production, Shaoxing 312000, China.

ARTICLE

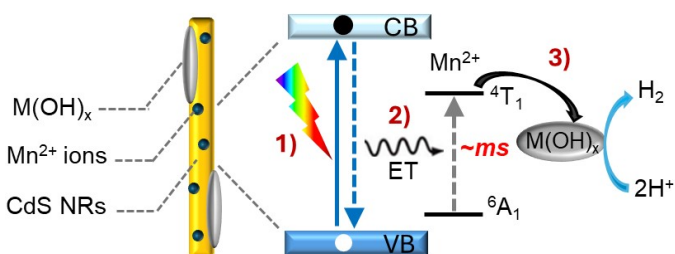
Journal Name

common photocatalytic conditions. Therefore, one such solution to controlling the oxidation state is to form more stable transition metal oxides and/or hydroxides.^{35-39,41-45} Metal hydroxides, $M(OH)_x$, offer a low-cost alternative to noble metals while having a relative inexpensiveness and high electron transfer ability with low hydrogen production overpotential.^{37,47-53}

Several metal hydroxides such as $Ni(OH)_2$ and $Co(OH)_2$ have been utilized as co-catalysts with CdS-based nanohybrids. A proposed mechanism is electron transfer from CdS to reduce the metal of the metal hydroxides (*i.e.*, Ni^{2+} to Ni^0 metal) for photocatalysis, followed by regeneration of the metal hydroxide as the redox active species takes the electron from the reduced metal.⁵⁴ Furthermore, $Ni(OH)_2$ has been noted for its ability to weaken the H–O bond in water for increased H_2 evolution.^{36,54,55} Additional approaches to utilizing CdS and $Ni(OH)_2$ nanohybrids are to physically separate the CdS and $Ni(OH)_2$ NPs with reduced graphene oxide to prevent NP agglomeration and increase photocatalytic hydrogen generation.⁴⁴ $Ni(OH)_2/Fe(OH)_x$ 0D NPs, (layered double hydroxides) have been formed on 1D CdS NRs for enhanced photocatalytic hydrogen generation due to the Fe acting as a redox mediator for the redox cycle at the Ni active site.⁴⁵ Cobalt hydroxides have also been utilized as co-catalysts with CdS with the co-catalyst providing enhanced photocatalytic hydrogen generation rates due to its ability to act as an electron acceptor and active site.^{52,56} Interestingly, previous work has noted $Co(OH)_2$ NPs as hole trapping sites in their photocatalytic systems for CO_2 reduction.⁵³ The use of metal hydroxides as co-catalysts is a desirable field of study due to the relative abundance of the first row transition metals and hydroxides coupled with their ability to act as an active site for photocatalysis. However, generally, lower photocatalytic performance of $Ni(OH)_2$ and $Co(OH)_2$ co-catalyst decorated CdS occurs when compared to Pt and other noble metals. This likely is due to 1) stability issues present in transition metals active sites arising from the ease of transition metals having oxidation state changes, and 2) less efficient electron transfer from CdS to the co-catalyst when comparing conductive noble metals with semiconductor transition metal hydroxides.

The use of dopants can offer an additional relaxation pathway by creating long-lived excitons through host-to-dopant energy transfer. Mn(II) dopants introduce discrete atomic energy levels (4T_1 and 6A_1) within the band gap of CdS. The spin-forbidden d-d transition (4T_1 and 6A_1) produces an orange emission centered at ~600 nm with a long lifetime (~ms),^{12,57-59,61-70} which is closer to the timescale of surface photocatalytic reactions (~ms–s).¹² Mn dopants have also been utilized for energy transfer donors as Mn(II) doped NCs wrapped in SiO_2 were able to interact with Pt NP co-catalyst by the Mn(II) dopants transferring energy to Pt co-catalysts for singlet oxygen generation.⁷¹ Based on our previous study, Mn dopants can act as a bridge between CdS and Pt, funnelling excitons from CdS to the Pt co-catalyst for enhanced photocatalytic redox activity.¹² Therefore we hypothesize that the use of Mn(II) dopants could also act as a bridge in noble metal free, earth abundant $M(OH)_x$ photocatalysts, including Mn:CdS- $M(OH)_x$ ($M = Ni^{2+}, Co^{2+}, Fe^{3+}$).

In this report, we utilized Mn(II) dopants in 1D CdS NRs which were then decorated with metal hydroxides, $M(OH)_x$ ($M = Ni^{2+}, Co^{2+}$, and Fe^{3+}), (*i.e.*, Mn:CdS- $Ni(OH)_2$, Mn:CdS- $Co(OH)_2$, and Mn:CdS- $Fe(OH)_3$, respectively), for photocatalysis.



Scheme 1. Schematic illustration of the excitonic and energy transfer processes in Mn(II) doped CdS NRs decorated with $M(OH)_x$ ($M = Ni^{2+}$, Co^{2+} , and Fe^{3+}) for H_2 generation. It should be noted the Mn²⁺ ions are oversized for clarity. (1) Photoexciting an electron from the valence band (VB) to the conduction band (CB), (2) energy transfer (ET) from the host CdS NR to Mn²⁺ dopants, and (3) electron transfer from dopants (with ~ms lifetime) to active sites of $M(OH)_x$ ($M = Ni^{2+}$, Co^{2+} , and Fe^{3+}) for H_2 generation from water splitting.

Upon the addition of metal hydroxides to the CdS NRs, the photocatalytic hydrogen generation under blue light irradiation increased by 52 times (52.1 vs 1.0 mmol/g/h, pH = 7), 2.5 times (20.5 vs 8.2 mmol/g/h, pH >13), and 3.1 times (25.4 vs 8.2 mmol/g/h, pH >13) for CdS- $Ni(OH)_2$, CdS- $Co(OH)_2$, and CdS- $Fe(OH)_3$, respectively. Aided by the ~1.0 ms lifetime of the excited electrons associated with the Mn(II) dopants, adding $M(OH)_x$ to the Mn:CdS NRs further enhanced the photocatalytic hydrogen yield by 2.1 times (112.0 mmol/g/h), 2.9 times (59.5 mmol/g/h), and 2.2 times (56.1 mmol/g/h), for Mn:CdS- $Ni(OH)_2$ (pH = 7), Mn:CdS- $Co(OH)_2$ (pH >13), and Mn:CdS- $Fe(OH)_3$ (pH >13), respectively. The long lifetime of the dopants can increase charge separation and provide a bridging pathway for efficient photocatalysis on $M(OH)_x$ co-catalysts. To the best of our knowledge, this is the first report of noble-metal-free $M(OH)_x$ co-catalyst-modified Mn(II)-doped CdS NRs for photocatalytic hydrogen evolution, and the first demonstration of $Fe(OH)_3$ as an effective co-catalyst in CdS-based hybrid photocatalysts.

Experimental

Chemicals. Cadmium oxide (CdO, ≥99.0%, Sigma-Aldrich), sulfur (99.998%, Sigma-Aldrich), 1-tetradecylphosphonic acid (TDPA, 98%, Sigma-Aldrich), trioctylphosphine oxide (TOPO, 99%, Alfa-Aesar), trioctylphosphine (TOP, 90%, Sigma-Aldrich), chloroform (99.8 %, Fisher-Scientific), Mn(II) acetate anhydrous (99.99%, Alfa-Aesar), oleylamine (Oam, 70%, Sigma-Aldrich), oleic acid (OA, 90%, Sigma-Aldrich), 3-mercaptopropionic acid (MPA, 99%, Alfa Aesar), tetramethylammonium hydroxide (TMaOH, 98%, Alfa Aesar), sodium hydroxide (NaOH, 98%, Thermo-Fisher), methanol (≥99%, VWR), toluene (≥99.5%, EMD Chemicals), ethanol (≥99%, anhydrous, Pharmco), acetone (≥99.5%, Sigma-Aldrich), ethyl acetate (≥99%, ACROS), hexane (99%, EMD), isopropyl alcohol (IPA ≥99.5% Sigma-Aldrich), nickel nitrate hexahydrate (99.9985%, STREM), cobalt nitrate hexahydrate (99%, Thermo-

Fisher), and ferric nitrate nonahydrate (98.5%, Fisher-Scientific). Deionized water was used in all experiments. All chemicals were used as purchased without further purification. **Synthesis of 1D CdS NRs.** 1D CdS NRs were synthesized based on a slightly modified literature reference.⁷² Cadmium and sulfur precursor solutions were first prepared separately. The cadmium precursor solution was prepared by mixing 115 mg (0.45 mmol) CdO, 415 mg (0.75 mmol) TDPA, and 3.5 g TOPO in a 50 mL flask and degassing for 1.5 h at 80 °C. The flask was then heated to 340 °C under Ar flow to form a Cd-TDPA complex indicated by a change in solution color from dark red to optically clear and then cooled to 300 °C. The sulfur precursor solution (S-TOP solution) was prepared by dissolving 110 mg (3.4 mmol) of sulfur powder in 10 mL of degassed TOP.

For the synthesis of 1D CdS NRs, 3 mL of the room temperature S-TOP precursor solution was injected into the hot Cd-TDPA solution at 300 °C, and the temperature of the reaction mixture dropped after addition and then ramped back to 300 °C in ~10 min. The remaining S-TOP (~7 mL) solution was injected, 1 mL at a time, every 5 minutes over a 35-minute period, the reaction then proceeded for an additional 30 minutes. At the end of the reaction, the solution was removed from the heating mantle and allowed to cool to approximately 60 °C and then 2-3 mL of chloroform was added to prevent solidification of the crude solution. The CdS NRs were separated from the crude solution by precipitating the particles with ethanol and centrifuging, then dispersed in hexane for optical measurements. The precipitate was further purified once by resuspending the NRs in toluene and then reprecipitating with ethanol and centrifuging for the growth of Pt tips.

Synthesis of 1D Mn:CdS NRs. The Mn(II) dopant precursor (Mn-TOP) was prepared inside a glovebox, where typically, 12 mg (0.04 mmol) of Mn(acetate) anhydrous and 1 mL of TOP were added to a flask. Then the solution was placed under vacuum for 30 minutes. The solution was further sonicated right before use to ensure the Mn(acetate) was fully dissolved.

The synthesis of Mn:CdS NRs followed a similar procedure used for CdS NRs except dropwise addition of the 1 mL Mn-TOP precursor into Cd-TDPA solution at 300 °C and allowed to settle for ~10 minutes. In addition, 9 mL S-TOP (instead of 10 mL S-TOP used in the synthesis of CdS NRs to keep the total volume of the TOP and the reaction the same volume as the undoped CdS NRs) with 2.7 mL of S-TOP is injected first step followed by injecting 0.9 mL every 5 minutes, the reaction then was allowed to proceed for an additional 30 minutes. The same purification method was used as in the undoped CdS NRs.

Ligand exchange. To make water soluble NRs, MPA ligand exchange was performed. Excess amount of MPA (1 mL) was dissolved in 5 mL methanol and the pH of the solution was adjusted to above 12 with TMaOH. The as-synthesized NRs (typically 0.23 mmol) were dispersed in 5 mL hexane and added to the above 5 mL MPA ligand solution in methanol. The solution was stirred overnight in aluminum foil wrapped containers. The MPA capped NRs were precipitated with ethyl acetate and isolated by centrifugation. The precipitate was further purified twice by resuspending the NRs in methanol and then reprecipitating with ethyl acetate and centrifuging.

Synthesis of hybrid 1D Mn:CdS-Ni(OH)₂ nanocomposites. The 1D Mn:CdS-Ni(OH)₂ hybrid photocatalysts were synthesized according to a literature method.³⁷ First, 0.23 mmol of the ligand exchanged, water soluble CdS NRs were dispersed in 5 mL of 0.05 M NaOH aqueous solution, and then a certain volume of 0.05 M Ni(NO₃)₂ aqueous solution (typically, 1.1 mL, 0.055 mmol; molar ratio between CdS:Ni(OH)₂ 1:0.23) was added dropwise under stirring. The resulting mixture was stirred for a certain amount of time at room temperature (typically one hour). After that, the precipitate was washed three times with deionized methanol and ethyl acetate.

Synthesis of hybrid 1D Mn:CdS-Co(OH)₂ nanocomposites. The synthesis of 1D Mn:CdS-Co(OH)₂ hybrid photocatalysts followed a previously reported method⁵² except the 0.05 M Ni(NO₃)₂ aqueous solution is replaced with 0.05 M Co(NO₃)₂ aqueous solution, the typical reaction time is raised to three hours, and the typical molar ratio is raised to (1:0.25).

Synthesis of hybrid 1D Mn:CdS-Fe(OH)₃ nanocomposites. The synthesis of 1D Mn:CdS-Fe(OH)₃ hybrid photocatalysts followed the previously mentioned method except the 0.05 M Ni(NO₃)₂ aqueous solution is replaced with 0.05 M Fe(NO₃)₃ aqueous solution, the typical reaction time is two hours, and the typical molar ratio is changed to (1:0.35).

Characterization. Powder X-ray diffraction (XRD) patterns were taken on a Bruker D2 Phaser with a LYKXEYE 1D silicon strip detector using Cu K α radiation ($\lambda = 1.5406 \text{ \AA}$). Transmission electron microscopy (TEM) images and high-resolution (HR-TEM) images were obtained on JEM 2100F (operated at an accelerating voltage of 200 kV). The UV-Visible (UV-Vis) absorption measurements were collected on an Agilent Cary 60 spectrophotometer. The photoluminescence (PL) measurements were performed with a Horiba FluoroMax Plus spectrofluorometer. Time-resolved emission measurements were conducted using an Edinburgh FLS-980 spectrometer with a photomultiplier tube (PMT, R928 Hamamatsu) detector. For NR bandgap PL lifetime measurements, the pulsed excitation light (365 nm) was used by an Edinburgh EPL-405 pulsed laser diode operating at a repetition rate of 0.2 MHz. For Mn²⁺ emission lifetime measurements, the pulsed excitation light was generated by an μ F2 60 W xenon flashlamp operating at a repetition rate of 20 Hz. Elemental composition analysis was performed on a PerkinElmer Avio 220 Max inductively coupled plasma-optical emission Spectrometer (ICP-OES). X-ray photoelectron spectroscopy (XPS) analysis was performed using a Thermo Scientific KAlpha+ instrument operating on an Al K α radiation (1486.6 eV). All XPS spectra were calibrated by using the carbon 1s peak at 284.8 eV. Room-temperature X-band EPR spectra were recorded on a Bruker ELEXSYSII E500 spectrometer at a microwave frequency of 9.8 GHz. For electrochemical measurements, a Gamry Interface 1010E electrochemical workstation was used, and the measurements were performed in a three-electrode setup with the sample electrode as the working electrode, platinum wire as the counter electrode, and Ag/AgCl (0.1 M NaClO₄, E_{Ag/AgCl} = +0.194 V vs. NHE) as the reference electrode. For cyclic voltammetry measurements (CV), a scan rate of 50 mV/s was utilized over the range of interest. Electrochemical impedance spectra (EIS) were



ARTICLE

Journal Name

measured in 0.1 M Na₂SO₄ at 1.2 V vs NHE with an amplitude of 25 mV (frequency: 100 mHz–100 kHz) under ambient lighting conditions. The electrochemical electrolyte was degassed for 30 min by flushing with high purity argon prior to CV and EIS measurement. Photocurrent measurements were taken in water at a neutral pH with constant stirring, and a working electrode of FTO glass with an area of 2.4 cm². The concentration of the NRs was kept constant by optical absorbance spectroscopy, and the light source was blue light LEDs 405 nm LEDs ($\lambda_{\text{max}} = 405 \pm 15 \text{ nm}$, 0.675 W).

Photocatalytic generation of hydrogen gas. 250 μL (0.009 mg) MPA-ligand exchanged NRs in distilled water, with a stock solution absorbance optical density of 26 at the first exciton peak, were added to a 15 mL glass centrifuge tube with a stir bar and 2.25 mL distilled water. To each reaction tube, 2.5 mL of isopropyl alcohol was added as a sacrificial hole scavenger. When the pH is kept neutral (pH = 7), 600 μL of DI water were added to the reaction tube, when the pH is adjusted to a basic solution (pH > 13), 600 μL of 0.1M NaOH were added to the reaction tube. The sample solutions were then vacuumed and refilled with Ar gas. The photochemical reactions were performed in a photochemical reactor equipped with 405 nm LEDs ($\lambda_{\text{max}} = 405 \pm 15 \text{ nm}$, 0.675 W) under stirring at 1000 rpm which was kept at room temperature by using cold water to prevent heating of the reaction tubes. The volume of the H₂ gas generated was collected in a burette and recorded periodically.

Results

Synthesis and Structure of M(OH)_x (M = Ni²⁺, Co²⁺, and Fe³⁺). In this study, we synthesized Mn(II) doped 1D CdS NRs decorated with M(OH)_x (i.e., Mn:CdS-M(OH)_x NRs, M = Ni²⁺, Co²⁺, and Fe³⁺) to study the role of dopants and co-catalysts on CdS-based photocatalytic performance. Firstly, 1D Mn:CdS NRs were synthesized via a hot-injection method by injecting S-precursor into Cd and Mn-precursor in TOP/TOPO solution at 300 °C. The undoped CdS NRs were also synthesized for comparison with the same procedure without adding the Mn precursor in the reaction. The as-obtained Mn:CdS NRs were then ligand exchanged to be water soluble with 3-mercaptopropionic acid and then decorated with M(OH)_x through M(NO)_x (M = Ni²⁺, Co²⁺, and Fe³⁺) precipitation in deionized water at room temperature.

The structure and morphology of the 1D CdS NR-based photocatalysts were characterized by XRD and TEM. The XRD patterns of the undoped and Mn(II) doped CdS NRs, as well as the Mn:CdS-Ni(OH)₂ indicates hexagonal phase 1D CdS NRs (Figure 1a). The (002) diffraction peak is more intense when compared with the standard hexagonal CdS XRD pattern, indicating cylindric growth of non-spherical NCs along the [001] direction (perpendicular to the (002) plane). After adding Ni(OH)₂ to the surface of the Mn:CdS NRs, new XRD peaks are present at 19.2°, 33.4°, ~38.7°, and 59.4° which can be assigned as the (001), (100), (101), and the (102) planes of Ni(OH)₂, respectively (Figure 1a) indicating successful growth of Ni(OH)₂ on the Mn:CdS NRs. The XRD patterns of M(OH)_x (M = Co²⁺ and Fe³⁺) co-catalyst modified NRs are shown in Figure S2a. After adding either Co(OH)₂ or Fe(OH)₃ to the surface of the Mn:CdS

NRs, however, no significant new XRD peaks are present. This might be due to the small amount of co-catalyst growth on the NRs; a similar lack of XRD patterns are present in previous reports of Co(OH)₂ and Fe(OH)₃ (Figure S2a).^{73–76}

The TEM images (Figure 1b and c) of the as-synthesized samples show CdS and Mn:CdS to be 1D cylindrical NRs with average diameter of $4.1 \pm 0.5 \text{ nm}$ and $4.0 \pm 0.5 \text{ nm}$, and an average length of $65 \pm 10 \text{ nm}$ and $65 \pm 10 \text{ nm}$, respectively (Figure S1). Based on the TEM images and histogram analysis (Figure S1) there is no significant difference in either the diameter and/or the length of the NRs with the addition of Mn(II) dopants. The TEM image of Mn:CdS-Ni(OH)₂ indicates the growth of the Ni(OH)₂ islands on the surface of the Mn:CdS NR (Figure 1d and e). The HR-TEM image of the Mn:CdS-Ni(OH)₂ (Figure 1f) shows a lattice fringe of 0.33 nm from the CdS NR, consistent with the (100) plane of hexagonal CdS, while the Ni(OH)₂ shows a lattice fringe of 0.23 nm consistent with the (101) plane of Ni(OH)₂. Due to the growth of Ni(OH)₂ onto the surface of the CdS NRs, the NRs are less uniform in diameter with a larger size distribution ($4.0 \pm 1.0 \text{ nm}$).

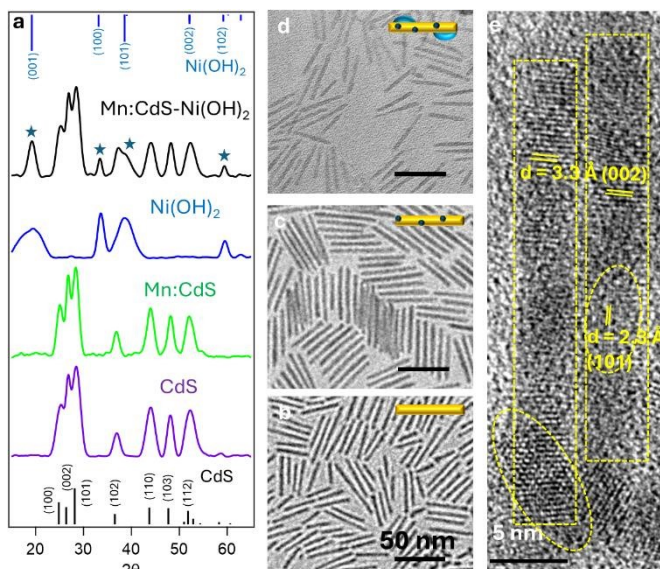


Figure 1. a) The x-ray diffraction (XRD) patterns for the CdS, Mn:CdS, and Mn:CdS-Ni(OH)₂ NRs. The presence of Ni(OH)₂ on Mn:CdS is indicated by a (★). b) TEM image of CdS NRs, c) TEM image of Mn:CdS NRs, and d) TEM image of Mn:CdS-Ni(OH)₂ NRs. e) HR-TEM image of Mn:CdS-Ni(OH)₂ showing the growth of Ni(OH)₂ on the Mn:CdS NRs showing the lattice fringes of CdS (0.33 nm [002] plane of CdS) and Ni(OH)₂ (0.23 nm [101] Ni(OH)₂). The dotted lines added to draw the viewer's eye.

The TEM images of Mn:CdS-M(OH)_x (M = Co²⁺ and Fe³⁺) indicate successful growth of M(OH)_x (M = Co²⁺ and Fe³⁺) on the surface of the Mn:CdS NRs (Figure S2c and b). The TEM and HR-TEM images indicate the successful growth of M(OH)_x (M = Co²⁺ and Fe³⁺) as a clear lattice fringe of 2.3 Å and 2.4 Å for Co(OH)₂ and Fe(OH)₃, respectively can be observed (Figure S2d and e) corresponding to the (101) planes of both Fe(OH)₃ and Co(OH)₂ (Figure S2a). The presence of the CdS (3.3 Å) NRs is also indicated by the HR-TEM lattice fringe for each sample further

suggesting successful Mn:CdS-M(OH)_x (M = Co²⁺ and Fe³⁺) formation.

ICP-OES measurements determined the concentration ratio between Ni and Cd for Mn:CdS-Ni(OH)₂ NRs and, a proxy for the concentration of Ni(OH)₂ and CdS, to be 0.11:1 indicating that roughly half the Ni(NO₃)₂ is converted to Ni(OH)₂ and that Ni(OH)₂ is present with the CdS NRs (Table S1). Similar conversion trends are observed for Mn:CdS-Co(OH)₂ and Mn:CdS-Fe(OH)₃ NRs with measured ratios of 0.12:1 and 0.16:1 for Co(OH)₂ and Fe(OH)₃, respectively on Mn:CdS NRs also indicating that Co(OH)₂ and Fe(OH)₃ were successfully formed (Table S1). ICP measurements indicate the same Mn(II) doping efficiency (0.9% Mn dopants) in the M(OH)_x (M = Ni²⁺, Co²⁺, and xFe³⁺) co-catalyst decorated Mn:CdS NRs, which corresponds to ~107 Mn(II) ions per NR.

The survey XPS spectrum (Figure S3a) of the Mn:CdS NRs shows distinct peaks for Cd 3d, S 2s, and Mn 2p, with the Cd 3d peaks at 406.0 eV (3d_{5/2}) and 412.8 eV (3d_{3/2}) (Figure S3e), the S 2p peaks at 162.4 eV (2p_{3/2}) and ~163 eV (2p_{1/2}) (Figure S3f), and the Mn(II) dopant peak at 652.3 eV (2p_{1/2}) (Figure S3g), consistent with the literature reported values.⁷⁷ Mn:CdS-M(OH)_x NRs (M = Ni²⁺, Co²⁺, and Fe³⁺) have similar peaks present for Mn, Cd, and S (Figure S3e, g, and f). The Mn:CdS-Ni(OH)₂ NRs have new peaks present from Ni(OH)₂ with 2p peaks at 861.3 eV and 855.7 eV (2p_{3/2}) and 878.1 and 873.4 eV (2p_{1/2}) (Figure S3b), the Mn:CdS-Co(OH)₂ NRs have new peaks present from Co(OH)₂ with 2p peaks at 789.3 eV and 782.1 eV (2p_{3/2}) and 807.1 and 799.8 eV (2p_{1/2}) (Figure S3c), and the Mn:CdS-Fe(OH)₃ NRs have new peaks present from Fe(OH)₃ with 2p peaks at 789.3 eV and 782.1 eV (2p_{3/2}) and 807.1 and 799.8 eV (2p_{1/2}) (Figure S3d), which are consistent with literature reported values.⁷⁸⁻⁸² The Mn, Cd, and S peaks exhibit a small peak shift (0.5±0.1 eV for Mn 2p_{1/2}, 0.3±0.1 eV for Cd 3d_{5/2} and 3d_{3/2}, and 0.2±0.1 eV for 2p_{3/2}) when comparing the Mn:CdS NRs with the M(OH)_x (M = Ni²⁺, Co²⁺, and Fe³⁺) decorated Mn:CdS NRs, which indicates that the electrons in both the CdS host CB and the Mn²⁺ dopant energy level are interacting with the M(OH)_x (M = Ni²⁺, Co²⁺, and Fe³⁺). As the distance between the Cd 3d_{5/2} and Cd 3d_{3/2} peaks stays consistent at 6.8 eV, this is further indication that electrons are transferring from the Mn:CdS NRs to the noble metal free M(OH)_x (M = Ni²⁺, Co²⁺, and Fe³⁺) co-catalysts.¹²

Optical properties. Figure 2a shows the absorption (dotted lines) and emission (solid lines) spectra of the 1D CdS, Mn:CdS, Mn:CdS-Ni(OH)₂, Mn:CdS-Co(OH)₂, and Mn:CdS-Fe(OH)₃ NRs. The first exciton absorption peak for all NRs is at ~470 nm from CdS, corresponding to a 2.6 eV bandgap. For CdS and Mn:CdS NRs, the CdS bandgap PL is at 480 nm and a broad defect emission peak centered around ~650 nm is also present, with PL QYs of 6.3% and 7.4%, respectively. There is no clear Mn(II) emission (~600 nm) present in the Mn:CdS NRs, which might be due to the large amount of surface trapping states considering the large surface to volume ratio of a 1D NR. The PL for Mn:CdS-Ni(OH)₂, Mn:CdS-Co(OH)₂, and Mn:CdS-Fe(OH)₃ does not have a clear emission showing the electron transfer from Mn:CdS to M(OH)_x (M = Ni²⁺, Co²⁺, and Fe³⁺) and PL QY decreases to <1% for each NR as well (Figure 2a).

The lifetimes for the CdS band edge PL at ~480 nm of the NRs are shown in Figure 2c: 5.6 ns for CdS, 4.9 ns for Mn:CdS, 1.9 ns for Mn:CdS-Ni(OH)₂, 2.6 ns for Mn:CdS-Co(OH)₂, and 2.8 ns for Mn:CdS-Fe(OH)₃ NRs (Figure 2c and Table S1). To reveal if there is direct electron transfer from Mn dopants to M(OH)_x co-catalysts, the lifetimes for the M(OH)_x decorated undoped NRs (*i.e.*, CdS-M(OH)_x (M = Ni²⁺, Co²⁺, and Fe³⁺) were measured, which show lifetime of 3.6 ns for CdS-Ni(OH)₂, 4.2 ns for CdS-Co(OH)₂, and 4.3 ns for CdS-Fe(OH)₃ (Figure S4 and Table S1, see SI for information on synthesis and characterization details).

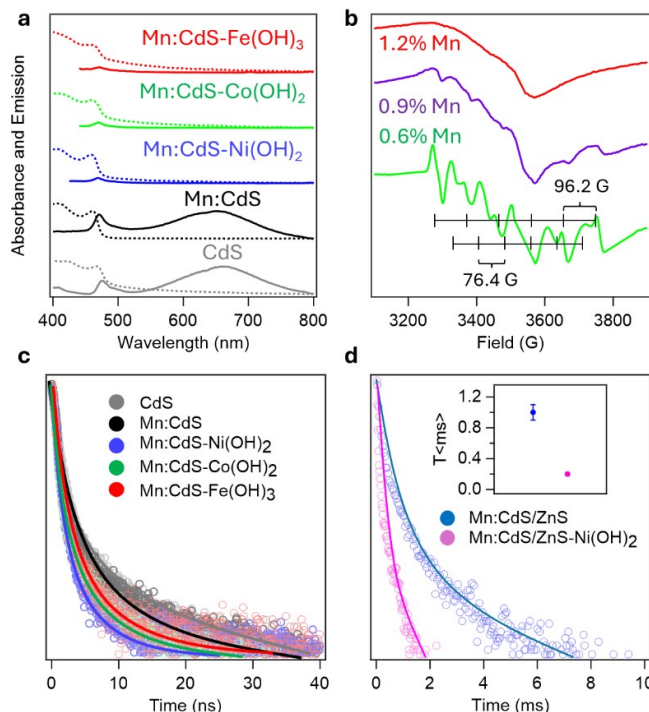


Figure 2. a) The absorption (dotted line) and emission (solid line) spectra for the CdS, Mn:CdS, Mn:CdS-Ni(OH)₂, Mn:CdS-Co(OH)₂, and Mn:CdS-Fe(OH)₃ NRs. b) EPR spectra of the 0.6%, 0.9%, and 1.2% Mn doped CdS NRs showing two sets of hyperfine peak splitting values with 96.2 G for surface Mn and 76.4 G for core Mn. c) Band edge PL lifetime emission spectra for CdS, Mn:CdS, Mn:CdS-Ni(OH)₂, Mn:CdS-Co(OH)₂, and Mn:CdS-Fe(OH)₃ NRs. d) PL Mn lifetime emission spectra for core/shell Mn:CdS/ZnS and Mn:CdS/ZnS-Ni(OH)₂ NRs.

Compared with undoped CdS NRs, the shorter band-edge PL lifetime observed for Mn:CdS NRs (5.6 ns vs 4.9 ns, Figure 2c) is attributed to host-to-Mn(II) dopant energy transfer, which introduces an additional relaxation pathway for photogenerated charge carriers (Scheme 1). There is a further decrease in the band edge PL lifetime when comparing the M(OH)_x decorated undoped CdS NRs (3.6 – 4.3 ns) with the lifetimes of their Mn doped counterparts (1.9 – 2.8 ns), which suggests the additional Mn(II) to M(OH)_x (M = Ni²⁺, Co²⁺, and Fe³⁺) relaxation pathway by electron transfer (Figure 2c and Table S2). Therefore, the Mn(II) dopants with longer PL lifetime (Figure 2d and S6) could enhance the electron transfer from the 1D CdS NRs to Ni(OH)₂.

Mn(II) dopants play an important role in the photocatalytic yields of the hybrid nano-photocatalysts (see further discussion of Mn(II) dopant concentration dependent photocatalytic



ARTICLE

Journal Name

performance in Discussion section). The presence of Mn(II) dopants within the CdS host lattice was also confirmed by X-band EPR spectroscopy (Figure 2b). In the Mn:CdS NRs, there are two sets of six-peak hyperfine splitting patterns with hyperfine constants (*A*) of 96.2 and 76.4 G, corresponding to the Mn(II) ions on the surface and the core of the CdS lattice, respectively. As the ICP measured concentration of the Mn(II) dopants increases from 0.9% to 1.2% (Figure 2b) the hyperfine peaks splitting patterns are less pronounced and eventually lost due to the concentration quenching effect.⁸³⁻⁸⁵

To better observe the Mn dopant emission (~600 nm) and determine the lifetime of the excited electrons associated with Mn(II) dopants, control experiments of a ZnS surface passivated Mn:CdS NRs and Mn:CdS/ZnS-Ni(OH)₂ NRs were performed to remove surface defects and therefore the broad surface defect emission (~650 nm). The resulting core/shell Mn:CdS/ZnS NRs show a clear Mn(II) dopant emission at ~600 nm (Figure S5a), however, the emission profile is gone upon the addition of Ni(OH)₂ (Figure S5a, see SI for information on synthesis and characterization details).

The Mn(II) emission lifetime from the Mn:CdS/ZnS core/shell NRs is ~1.0 ms, which decreases to ~0.2 ms upon Ni(OH)₂ decoration in the Mn:CdS/ZnS-Ni(OH)₂ NRs (Figure 2d). The pronounced decrease in Mn(II) emission lifetime upon deposition of Ni(OH)₂ indicates electron transfer from Mn(II) dopant states to the co-catalyst in the hybrid nanostructures. A similar charge-transfer pathway is expected for Co(OH)₂- and Fe(OH)₃-decorated Mn:CdS NRs. In addition, after ZnS shell coating, only a singular hyperfine peak splitting pattern is observed of 68 G from the core Mn(II) dopants was observed (Figure S5b), which proves the smaller EPR hyperfine splitting (76.4 G) arising from the core Mn(II) ions in CdS NRs.

Electrochemical properties. The charge transport resistance is a facsimile for the availability of electrons to participate in photocatalytic redox reactions, and therefore, the charge transport properties of the as-synthesized CdS, Mn:CdS, and Mn:CdS-M(OH)_x (M = Ni²⁺, Co²⁺, and Fe³⁺) NRs were studied by electrochemical impedance spectroscopy (EIS). In the EIS spectra, the smaller the semicircle arc, the better the potential for photocatalysis. As shown in Figure 3a, the Mn:CdS NRs have a smaller semicircle arc than CdS, demonstrating decreased charge transfer resistance for Mn:CdS NRs compared to CdS NRs, suggesting that the long-lived Mn(II) dopants are altering the charge recombination dynamics and allowing more electrons to participate in photocatalysis.

For comparison, Mn(II) doped and undoped CdS NRs decorated with M(OH)_x (M = Ni²⁺, Co²⁺, and Fe³⁺) were synthesized and the corresponding EIS plots are shown in Figure 3b. Further reduction of the charge transport resistance (smaller semicircle arc) was obtained by the growth of M(OH)_x islands on the Mn:CdS NRs (Figure 3a and b), with a general trend of Ni(OH)₂ < Co(OH)₂ < Fe(OH)₃ showing that Ni(OH)₂ is expected to give the largest photocatalysis followed by Co(OH)₂ and then Fe(OH)₃. Furthermore, decreased charge transport resistance from Mn:CdS-M(OH)_x (M = Ni²⁺, Co²⁺, and Fe³⁺) NRs suggests that the Mn(II) dopants can interact with M(OH)_x co-catalysts for enhanced photocatalysis. The as-calculated values

for R_s and R_{ct} for the NR photocatalysts (Table S3) show the decreased charge transfer resistance for the CdS-based NRs upon the addition of Mn(II) dopants.

Cyclic voltammetry (CV) was used to study the bandgap of each photocatalyst and thus the suitability of the 1D CdS NR-based photocatalysts for catalytic water reduction (Figure S6). The position of the conduction band can be measured by finding the onset of the current increase on the CV which occurs at ~-0.8 V vs NHE (Figure S6). Based on the calculated bandgap from the absorbance data, the position of the conduction band can be obtained; the CdS-based NRs show a bandgap of ~2.6 eV consistent with the absorption data in Figure 2a.

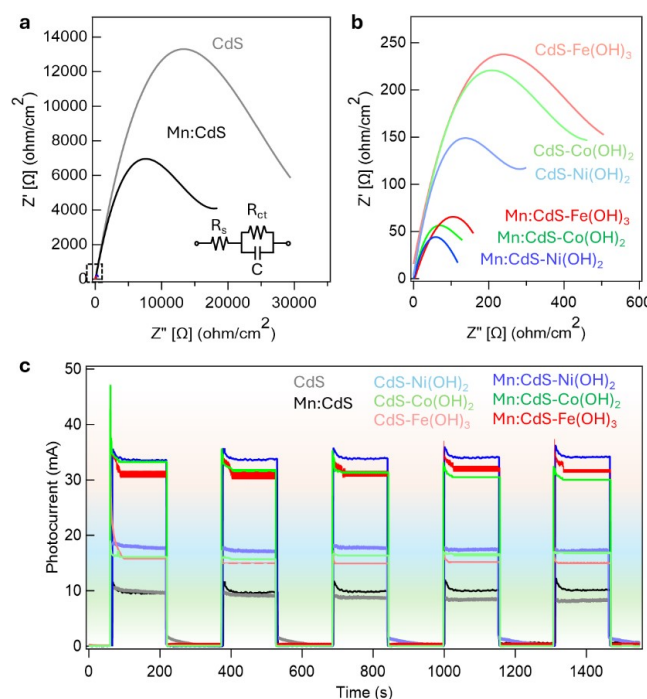


Figure 3. a) EIS spectra for CdS, Mn:CdS, CdS-M(OH)_x (M = Ni²⁺, Co²⁺, and Fe³⁺), and Mn:CdS-M(OH)_x (M = Ni²⁺, Co²⁺, and Fe³⁺) NRs. b) Zoomed in EIS spectra for the CdS-M(OH)_x (M = Ni²⁺, Co²⁺, and Fe³⁺) and Mn:CdS-M(OH)_x (M = Ni²⁺, Co²⁺, and Fe³⁺) NRs. c) Photocurrent measurements of CdS, Mn:CdS, and their corresponding co-catalyst M(OH)_x (M = Ni²⁺, Co²⁺, and Fe³⁺) decorated NRs.

There is not a significant change in the CV upon the addition of M(OH)_x (M = Ni²⁺, Co²⁺, and Fe³⁺) suggesting that the bandgap remains consistent at ~2.6 eV, further confirmed by the absorption data in Figure 2a and Figure S4a. Therefore, the bandgaps of each CdS-based NR (Figure S6) are wide enough to cover the 1.23 eV needed to split water and generate hydrogen gas. For the Mn(II) doped NRs, there is an increase in the area under the CV curve at ~0.8 V; this could be attributed to the presence of the Mn²⁺ dopants as the CV measures the available states for electrons to be added. The M(OH)_x NRs have a peak at roughly -0.4 V, -0.5 V, and -0.7 V for the Ni(OH)₂, Co(OH)₂, and Fe(OH)₃ decorated NRs, respectively, which can be attributed to the reduction process of forming Ni(0), Co(0), and Fe(0) metal, respectively.^{76,86-89}

Photocurrent measurements were performed for the CdS-based NRs (Figure 3c). The transient photocurrent responses

increased after the incorporation of Mn(II) dopants into the CdS NRs; there was a further significant photocurrent enhancement after $M(OH)_x$ ($M = Ni^{2+}$, Co^{2+} , and Fe^{3+}) decoration. This enhancement of the photocurrent response is consistent with the shorter band edge PL lifetime ($CdS > Mn:CdS > Mn:CdS-M(OH)_x$ ($M = Ni^{2+}$, Co^{2+} , and Fe^{3+})) (Figure 2c) showing additional electron relaxation pathways to the dopants and co-catalyst. The photocurrent responses also follow a general trend of $Ni(OH)_2 > Co(OH)_2 > Fe(OH)_3$ in the Mn(II) doped and undoped CdS NRs and is also consistent with the reduced charge transport resistance in $Mn:CdS-M(OH)_x$ ($M = Ni^{2+}$, Co^{2+} , and Fe^{3+}) NRs from the EIS data (Figure 3a and b).

Photocatalytic H_2 Generation by Water Splitting.

Photocatalytic hydrogen generation from water splitting experiments were conducted with the NRs under blue light LED ($\lambda_{max} = 405 \pm 15$ nm, 0.675 W) irradiation at room temperature with a neutral pH (pH = 7). Figure 4 shows the catalytic performance of the 1D CdS NR-based NRs. The CdS NRs generated 0.8 mmol/g/h of hydrogen gas, while the Mn:CdS NRs did not show notable hydrogen generation enhancement (1.0 mmol/g/h) under the same reaction conditions. This can be explained by the isolated Mn(II) dopants which are 1) not always on the surface of the CdS NRs (see EPR Figure 2b) and 2) the small portion of surface Mn(II) dopants could not provide enough active sites for water molecules, hence lower photocatalysis.

Upon the addition of $M(OH)_x$ ($M = Ni^{2+}$, Co^{2+} , and Fe^{3+}) co-catalysts, significant enhancement of the photocatalysis was achieved compared to the Mn:CdS NRs (1.0 mmol/g/h) of 108.2, 17.3, and 13.6 mmol/g/h of hydrogen generation for 1D $Mn:CdS-Ni(OH)_2$, $Mn:CdS-Co(OH)_2$, and $Mn:CdS-Fe(OH)_3$ NRs, respectively. In addition, without Mn(II) dopants 52.1, 11.0, and 4.0 mmol/g/h of hydrogen gas were generated from the $CdS-Ni(OH)_2$, $CdS-Co(OH)_2$, and $CdS-Fe(OH)_3$ NRs, respectively. Generally, the NRs follow a consistent trend of $Ni(OH)_2 > Co(OH)_2 > Fe(OH)_3$ when comparing the Mn(II) doped NRs with their undoped counterparts (*i.e.*, $Mn:CdS-Ni(OH)_2$ vs $CdS-Ni(OH)_2$); enhanced photocatalysis observed from the Mn(II) doped and/or co-catalyst decorated NRs is consistent with decreased charge transport resistance as measured in the EIS spectra (Figure 3a and b). Therefore, enhanced hydrogen generation arises from the synergistic effect between long lifetime Mn(II) dopants ($\sim ms$) (Figure 2d) and electron transfer to the co-catalyst resulting in electrons accumulating on the $M(OH)_x$ islands for subsequent photo-redox reactions.

Recycle tests were also performed to study the stability of the photocatalysts, in which the photocatalyst was re-collected and the photocatalytic solution was remade by adding the same amount of hole scavenger at the same pH (Figure 4b). The hour-by-hour recycling reaction using the same 1D $Mn:CdS-Ni(OH)_2$ photocatalyst revealed a stable ~95% performance of the previous photocatalytic result. The photocatalytic efficiency was maintained over the course of three cycles, highlighting the photostable recyclability for the photocatalyst. Recycle tests for Mn(II) doped CdS NRs decorated with $M(OH)_x$ ($M = Co^{2+}$ and Fe^{3+}) were also performed (Figure 4d and f). The $M(OH)_x$ (M

= Co^{2+} and Fe^{3+}) decorated NRs show limited stability during the recycle tests which might be due to the limited stability of $Co(OH)_2$ and $Fe(OH)_3$ in neutral pH during the sample cleaning and recycling processes (see effect of pH in the Discussion section).

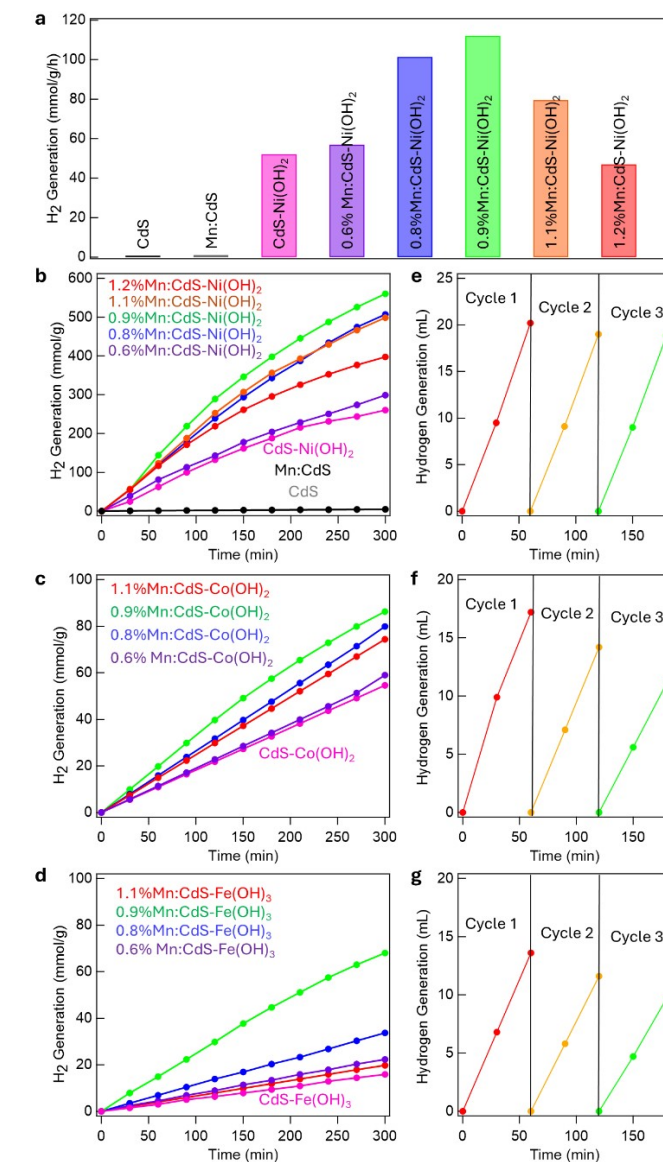


Figure 4. a) Average hydrogen generation of the $Mn:CdS-Ni(OH)_2$ NRs in mmol/g/h. Photocatalytic hydrogen generation of b) CdS, Mn:CdS, $CdS-Ni(OH)_2$, and $Mn:CdS-Ni(OH)_2$, c) $CdS-Co(OH)_2$ and $Mn:CdS-Co(OH)_2$, and d) $CdS-Fe(OH)_3$ and $Mn:CdS-Fe(OH)_3$ at neutral pH with differing Mn doping concentrations shown as % of Mn atoms per CdS NR. Recycle test for the e) $Mn:CdS-Ni(OH)_2$ NRs, f) $Mn:CdS-Co(OH)_2$ NRs, and g) $Mn:CdS-Fe(OH)_3$ NRs over three one-hour cycles.

Discussion

Photocatalytic Mechanism of the 1D $Mn:CdS-M(OH)_x$ Hybrid NRs. Figure 5a illustrates the host-to-dopant energy transfer and following electron transport to the $M(OH)_x$ co-catalyst in the 1D $Mn:CdS-M(OH)_x$ ($M = Ni^{2+}$, Co^{2+} , and Fe^{3+}) NRs for photocatalytic H_2 gas generation under blue light excitation. The interactions between the long lifetime Mn(II) dopants and

ARTICLE

Journal Name

the $M(OH)_x$ ($M = Ni^{2+}$, Co^{2+} , and Fe^{3+}) co-catalyst demonstrates the two-step nature of the charge carrier transport. Firstly, the CdS absorbs light (Figure 2a) from the photoreactor, then *Step 1* host-to-dopant energy transfer occurs creating long-lived lifetimes of the excitons (ms) on the $Mn(II)$ dopants. *Step 2* follows where electron transfer from either the host CdS (ns) or $Mn(II)$ dopants (ms), though likely more the $Mn(II)$ dopants due to the difference in photocatalytic hydrogen generation (Figure 4a, c, and d) and lifetime (Figure 2c, Figure S4b, and Table S2), to the co-catalyst $M(OH)_x$ ($M = Ni^{2+}$, Co^{2+} , and Fe^{3+}) for more efficient photocatalysis due to an increase in the lifetimes of the charge separated states.

The shorter CdS PL lifetime of the $Mn:CdS$ NRs compared to that of pristine CdS NRs (Figure 2c and Table S2) indicates the host-to-dopant energy transfer (*Step 1*). The following electron transfer (*Step 2*) from $Mn:CdS$ to $M(OH)_x$ ($M = Ni^{2+}$, Co^{2+} , and Fe^{3+}) is demonstrated by the decrease in PL QY after $M(OH)_x$ ($M = Ni^{2+}$, Co^{2+} , and Fe^{3+}) decoration (Figure 2a). In addition, the $Mn(II)$ dopant PL lifetime in the $Mn:CdS/ZnS$ type I core/shell NRs also decreases after growth of $Ni(OH)_2$ co-catalyst due to electron transfer from $Mn(II)$ dopants to $Ni(OH)_2$ (Figure 2d). Further evidence of two successive steps is demonstrated by the reduced charge transport resistance and enhanced charge transport from CdS to $Mn:CdS$ to $Mn:CdS-M(OH)_x$ ($M = Ni^{2+}$, Co^{2+} , and Fe^{3+}) NRs by EIS data (Figure 3a and b) and the photocurrent results (Figure 3c), respectively.

The longer lifetime $Mn(II)$ dopants function as a bridge between the light harvesting CdS and active site co-catalytic $M(OH)_x$ ($M = Ni^{2+}$, Co^{2+} , and Fe^{3+}) (by dopant to $M(OH)_x$ ($M = Ni^{2+}$, Co^{2+} , and Fe^{3+}) electron transfer) for enhanced charge transport, which leads to a greater hydrogen generation efficiency. The positions of the band edges of CdS , Mn^{2+} dopants, and the metals $Ni(0)$, $Co(0)$, and $Fe(0)$ (generated from the respective reduction of $M(OH)_x$ ($M = Ni^{2+}$, Co^{2+} , and Fe^{3+}), see below) are more negative vs NHE than the reduction potential of water,^{50,51,76,88-92} where these energy band levels are in a down-stepping structure moving the electrons to the $M(OH)_x$ ($M = Ni^{2+}$, Co^{2+} , and Fe^{3+}) for photocatalytic hydrogen generation from water splitting (Figure 5a).

Previous reports propose that $Ni(OH)_2$ undergoes self-reduction during photocatalysis to form isolated $Ni(0)$ atoms/small clusters on the surface of the CdS NR.^{50,51} These isolated $Ni(0)$ species act as active sites for hydrogen evolution while $Ni(OH)_2$ improves the mass transport of H_2O to the self-reduced $Ni(0)$.^{50,51} This process has also been reported for $Co(OH)_2$ ⁵² and in this first report of $Fe(OH)_3$ co-catalyst utilization in CdS -based photocatalysts, a similar photocatalytic mechanistic reduction of $Fe(OH)_3$ to $Fe(0)$ is proposed. Therefore, during photocatalysis, reduction of the co-catalyst $M(OH)_x$ ($M = Ni^{2+}$, Co^{2+} , and Fe^{3+}) to the metallic form occurs *in situ* before photocatalytic interaction with hydrogen in solution (Figure 5a). It should be noted that at the interface between the CdS semiconductor and the $M(OH)_x$ co-catalyst, Fermi-level equilibration leads to the formation of a Schottky barrier, inducing interfacial band bending and charge redistribution. This interfacial effect promotes efficient charge separation and suppresses recombination of photogenerated carriers.

Effect of pH. The photocatalytic performance of the $Ni(OH)_2$ decorated NRs (Figure 4a) follow the observed trends in the EIS spectra (Figure 3b) and PL lifetime (Figure 2c and S6), where the greatest expected photocatalytic performance is expected from $Mn(II)$ doped CdS NRs decorated with $Ni(OH)_2$, then $Co(OH)_2$, and $Fe(OH)_3$ followed by undoped CdS NRs decorated with $Ni(OH)_2$, then $Co(OH)_2$, and $Fe(OH)_3$. However, the $Mn:CdS-M(OH)_x$ ($M = Co^{2+}$ and Fe^{3+}) NRs had lower photocatalytic hydrogen generation than $CdS-Ni(OH)_2$ (Figure 4), which is inconsistent with the EIS spectra (Figure 3b) and PL lifetime (Figure 2c and S6). To understand these observed results, pH dependent photocatalysis of the ideal 0.9% $Mn(II)$ doped CdS $M(OH)_x$ ($M = Ni^{2+}$, Co^{2+} , and Fe^{3+}) co-catalyst decorated NRs were measured (Figure 5b).

The highest rate of photocatalysis for the $Mn:CdS-Ni(OH)_2$ NRs was at a neutral pH (pH = 7) (Figure 5c), while the highest rate of photocatalysis for the $Mn:CdS-Co(OH)_2$ (Figure 5d) and $Mn:CdS-Fe(OH)_3$ NRs (Figure 5e) was at a basic pH >13 (Figure 5b). A likely explanation for pH-dependent performance is due to the forms of the $M(OH)_x$ ($M = Co^{2+}$ and Fe^{3+}) are a function of pH, shown in Pourbaix diagram(s) (Figure 5f, g, and h).⁹⁴⁻⁹⁷ Figure 5f shows the thermodynamically favorable states of $Ni(OH)_2$ as a function of potential (V) vs NHE and pH.^{94,96-99} As the pH grows more basic, the form of $Ni(OH)_2$ that is most stable changes from Ni^{2+} , to $Ni(OH)_2$, to $Ni(OH)_3^-$ as the pH changes from acidic (pH ≈ 4), to neutral (pH = 7), to basic (pH > 13) (Figure 5f). However, for $Co(OH)_2$ and $Fe(OH)_3$, the stable form is either Fe^{2+} or Co^{2+} , respectively in acidic (pH ≈ 4) or neutral (pH = 7) conditions, while at more basic conditions (pH > 13), the metal hydroxide is formed for $Fe(OH)_3$ and $Co(OH)_2$, respectively (Figure 5g and h).

Therefore, the as-observed trends in Figure 4a, c, and e can be explained by the forms of the transition metal compounds. Both Ni^{2+} ^{100,101} and $Ni(OH)_2$ ^{37,44,49,86} are known to undergo photocatalytic hydrogen generation. However, $Ni(OH)_3^-$ has a negative charge and would likely have Columbic repulsion towards any photoexcited electron from $Mn:CdS$ resulting in lower photocatalysis. As the stable form of $Fe(OH)_3$ and $Co(OH)_2$ at all pH values is either the transition metal cation or metal hydroxide, there is no Columbic repulsion of photoexcited electrons. Since IPA hole scavenging is best at basic conditions¹⁰², the greatest photocatalytic enhancement for $Mn:CdS-Co(OH)_2$ and $Mn:CdS-Fe(OH)_3$ can occur at basic conditions. Crucially, the lack of a Columbic repulsive force on the metal hydroxide co-catalyst allows for more efficient electron transfer. This could also explain the lack of recycling stability for the $M(OH)_x$ ($M = Co^{2+}$ and Fe^{3+}) NRs as during the cleaning process, the solutions return to a neutral pH which could start the formation of side products and poison the photocatalyst (Figure 4d and f).



ARTICLE

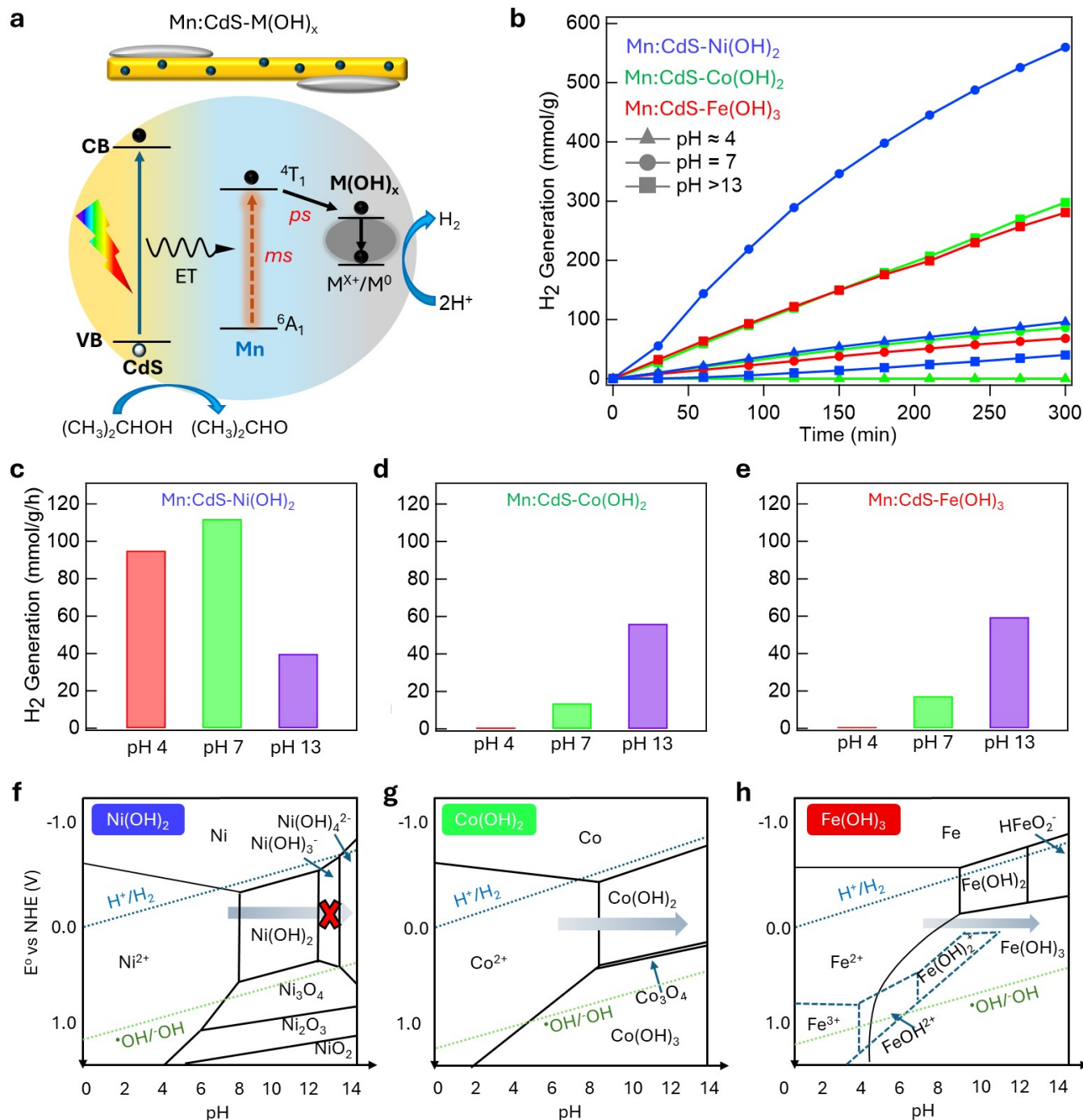


Figure 5. a) Schematic illustration of the host-to-dopant energy transfer and following electron transport to the $M(OH)_x$ co-catalyst with subsequent $M(X)$ to $M(0)$ ($M = Ni^{2+}$, Co^{2+} , and Fe^{3+}) self-reduction for photocatalytic hydrogen generation from water splitting in the 1D $Mn:CdS-M(OH)_x$ NRs at neutral pH. It should be noted the Mn^{2+} ions are oversized for clarity. b) pH dependent photocatalytic hydrogen generation of the $Mn:CdS-M(OH)_x$ ($M = Ni^{2+}$, Co^{2+} , and Fe^{3+}) decorated NRs. pH dependent photocatalysis of the $Mn:CdS-M(OH)_x$ ($M = c$ Ni^{2+} , d) Co^{2+} , and e) Fe^{3+}) NRs in mmol/g/h of hydrogen generated. Pourbaix Diagrams⁹⁵ showing the electrochemical stability of f) $Ni(OH)_2$ ⁹⁴, g) $Co(OH)_2$ ^{97,99}, and h) $Fe(OH)_3$ ^{96,98}.

ARTICLE

Figure 6a shows the catalytic performance of the Co(OH)_2 NRs for photocatalytic hydrogen generation from water splitting while Figure 6b shows the catalytic performance of the Fe(OH)_3 NRs. Under basic conditions, CdS generated 8.2 mmol/g/h of hydrogen gas, Mn:CdS generated 9.8 mmol/g/h of hydrogen gas. As IPA hole scavenging is more efficient under basic conditions¹⁰², the likelihood of Columbic forces preventing photocatalysis are lessened and therefore, the longer-lived lifetimes arising from Mn(II) dopants can perform better for the Mn:CdS NRs, contrasting with the poor performance of the Mn(II) doped and undoped CdS -based NRs at neutral conditions (Figure 4a).

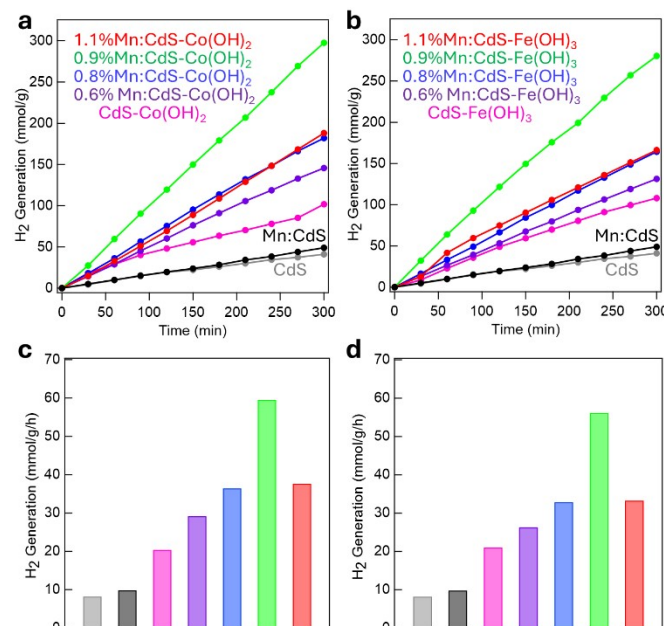


Figure 6. a) Photocatalytic hydrogen generation of CdS , Mn:CdS , CdS-Co(OH)_2 , and Mn:CdS-Co(OH)_2 under basic conditions ($\text{pH} > 13$) with differing Mn doping concentrations shown as % of Mn atoms per CdS NR. **b)** Photocatalytic hydrogen generation of CdS , Mn:CdS , CdS-Fe(OH)_3 , and Mn:CdS-Fe(OH)_3 under basic conditions ($\text{pH} > 13$) with the Mn doping concentrations shown as % of Mn atoms per CdS NR. Average hydrogen generation of the **c)** Mn:CdS-Co(OH)_2 and **d)** Mn:CdS-Fe(OH)_3 NRs in mmol/g/h, color coded with the results in a) and b). At basic pH (> 13), the 1D Mn:CdS-Co(OH)_2 NRs show an improvement of 3.4 times in overall hydrogen generation when compared with the neutral pH Mn:CdS-Co(OH)_2 NRs (59.5 mmol/g/h vs 17.3 mmol/g/h) (Figure 4c and 6a). The 1D Mn:CdS-Fe(OH)_3 NRs, show an enhanced photocatalytic hydrogen generation of 4.1 times greater than Mn:CdS-Fe(OH)_3 at neutral pH (56.1 vs 13.6 mmol/g/h) (Figure 4d and 6b). Notably, at higher and lower $[\text{Mn(II)}]$ dopants, the

photocatalytic efficiency is decreased for Mn:CdS-Co(OH)_2 and Mn:CdS-Fe(OH)_3 at both neutral and basic pH (Figure 4c and d and Figure 6a and b). The consistent photocatalytic hydrogen trends for the Mn(II) dopant concentration dependent photocatalysis (see discussion of Mn(II) dopant concentration photocatalysis) between neutral and basic pH suggests that the Mn(II) dopants can act efficiently as a bridge regardless of pH. Therefore, any changes in photocatalytic hydrogen generation rate are dependent upon the co-catalyst surface consistent with the explanation offered from the Pourbaix diagrams (Figure 5f, g, and h).

The increased photocatalytic hydrogen generation for Mn:CdS-Co(OH)_2 and Mn:CdS-Fe(OH)_3 upon changing the pH (Figure 5b) from neutral to basic demonstrates the importance of controlling the form of first row transition metal compounds (Figure 5c, d, and e). At pH values where the M(OH)_x is positive or neutrally charged from the Pourbaix diagrams (Figure 5f, g, and h), higher photocatalytic hydrogen generation is observed consistent with photocatalytic trends observed for Mn:CdS-Ni(OH)_2 (Figure 4a), Mn:CdS-Co(OH)_2 (Figure 4c and 6a), and Mn:CdS-Fe(OH)_3 (Figure 4d and 6b).

Mn(II) Dopant Concentration-Dependent Photocatalytic Performance. The role of Mn(II) dopants acting as a bridge between CdS and M(OH)_x ($\text{M} = \text{Ni}^{2+}$, Co^{2+} , and Fe^{3+}) was further elucidated by comparing the impact of Mn(II) doping concentration on the CdS NRs. First, a control experiments to determine the photocatalytic hydrogen generation of undoped CdS-M(OH)_x ($\text{M} = \text{Ni}^{2+}$, Co^{2+} , and Fe^{3+}) NRs was performed, with 52.1, 20.3, and 25.4 mmol/g/h of H₂ gas generated on CdS-Ni(OH)_2 (Figure 4a, pH 7), CdS-Co(OH)_2 (Figure 6a, pH 13), and CdS-Fe(OH)_3 NRs (Figure 6b, pH 13), respectively. To further reveal the Mn doping concentration-dependent performance of the hybrid catalysts, we also investigated the Mn doping concentration-dependent photocatalysis for Mn:CdS-M(OH)_x for $[\text{Mn}]$ between 0.6% and 1.2%. The maximum hydrogen generation yield occurs at 0.9% Mn(II) dopants in M(OH)_x decorated NRs with 112.0 mmol/g/h, 59.5 mmol/g/h, and 56.1 mmol/g/h for Mn:CdS-Ni(OH)_2 , Mn:CdS-Co(OH)_2 , and Mn:CdS-Fe(OH)_3 , respectively (Figure 4a and 6a and b).

At Mn(II) concentrations lower than the ideal Mn(II) concentration, there are less than an ideal number of energy transfer acceptors in the host-to-dopant energy transfer system. When the concentration of Mn(II) dopants is either 0.6% or 0.8% (< 0.9% in the previous results), the photocatalytic hydrogen yield is 56.9 and 101.4 mol/g/h, for 0.6% and 0.8% Mn doped Mn:CdS-Ni(OH)_2 ; 29.1 and 36.4 mmol/g/h for 0.6% and 0.8% Mn doped Mn:CdS-Co(OH)_2 ; and 26.2 and 32.8 mmol/g/h for 0.6% and 0.8% Mn doped Mn:CdS-Fe(OH)_3 ,

respectively. With limited (<0.9%) Mn(II) dopants available for host-to-dopant energy transfer, fewer excited excitons can transfer their energy to Mn(II) dopants, resulting in a limited increase in the photocatalytic hydrogen generation over pure CdS (Figure 4a and 6a and b). However, the lifetime of the Mn(II) PL lifetime stays relatively constant from 1.01 to 0.97 ms when the Mn(II) concentration decreases from 0.9% to 0.6% of the corresponding Mn:CdS/ZnS NRs (Figure S5c) suggesting that any decrease in photocatalysis does not come from a lack of ability of the Mn(II) dopants to effectively promote the lifetime of the charge separated states. Therefore, this highlights the important impact of having enough Mn(II) acceptors for efficient bridging; the severely isolated Mn(II) dopants cannot effectively shuttle electrons from photoexcited CdS to M(OH)_x (M = Ni²⁺, Co²⁺, and Fe³⁺) and as a result, effective photocatalysis cannot occur.

At higher Mn(II) concentrations than the ideal (>0.9%), short-range Mn-Mn interactions lead to a concentration quenching effect, as shown by a broad dipolar EPR peak without well-resolved hyperfine peaks (Figure 3d). The higher Mn doping concentration also therefore leads to reduced hydrogen generation with 1.05% Mn-doped Mn:CdS-M(OH)_x (M = Ni²⁺, Co²⁺, and Fe³⁺) having 79.5 mmol/g/h, 37.6 mmol/g/h, and 33.2 mmol/g/h for Mn:CdS-Ni(OH)₂, Mn:CdS-Co(OH)₂, and Mn:CdS-Fe(OH)₃, respectively (Figure 4a and 6a and b) as the concentration quenching reduces the number of long-lived charge carriers from being utilized in photocatalysis. Concentration dependent quenching is common at higher doping concentrations due to the cross-relaxation between Mn-Mn coupled dopants where the dopants are closer to each other.^{103,104} The concentration quenching effect can also be seen in the PL lifetime spectra of the Mn(II) doped core/shell Mn:CdS/ZnS NRs as the Mn(II) PL lifetime decreases from 1.01 to 0.87 ms when the Mn(II) concentration increases from 0.9% to 1.2% (Figure S5c and inset). Since the Mn(II) dopants provide an alternative relaxation pathway for the photoexcited electrons, it can be understood that fewer are available to undergo photocatalysis if concentration quenching occurs.

Decoration of Mn:CdS by M(OH)_x. The co-catalyst M(OH)_x (M = Ni²⁺, Co²⁺, and Fe³⁺) on the Mn:CdS-based NRs shows both time and concentration based photocatalytic dependence. In Figure S7 the hydrogen generation of M(OH)_x (M = Ni²⁺, Co²⁺, and Fe³⁺) at different reaction times is shown. The highest photocatalytic yield is observed for a one-hour reaction of Ni(OH)₂, for three hours on Co(OH)₂, and three-hours for Fe(OH)₃ on Mn:CdS. When the M(OH)_x (M = Ni²⁺, Co²⁺, and Fe³⁺) reaction time is half the ideal reaction time, the photocatalytic yield decreases by ~50%. At reaction times longer one-hour, from 1.5 hours to 7 hours, the photocatalytic hydrogen yield decreases as the reaction time increases until at 420+ minutes, the photocatalytic hydrogen yield even becomes negligible for M(OH)_x (M = Ni²⁺, Co²⁺). This can be understood by the reaction time controlling the total decoration of the M(OH)_x (M = Ni²⁺, Co²⁺, and Fe³⁺) on the Mn:CdS NRs. Below the ideal reaction times, not enough M(OH)_x decoration occurs; above the ideal reaction time, too much M(OH)_x (M = Ni²⁺, Co²⁺, and Fe³⁺)

growth occurs which likely blocks incident light from reaching CdS and undergoing charge separation for photocatalysis. There is also a similar concentration dependence between the Mn:CdS-Ni(OH)₂ NRs with differing M(OH)_x (M = Ni²⁺, Co²⁺, and Fe³⁺) concentrations. When the M(OH)_x (M = Ni²⁺, Co²⁺, and Fe³⁺) concentration was varied, the reaction time for the M(OH)_x (M = Ni²⁺, Co²⁺, and Fe³⁺) was kept constant at the respective ideals (1, 3, and 2 hours respectively Ni(OH)₂, Co(OH)₂, and Fe(OH)₃). Figure S8 shows the molar ratio dependence of the M(OH)_x (M = Ni²⁺, Co²⁺, and Fe³⁺) decoration as measured by ICP (see Table S1 and discussion in results section for more details on the calculation). For example, when the molar ratio between CdS and Ni(OH)₂ is less than 1 to 0.23, the rate of photocatalytic hydrogen evolution decreases, while above 1 to 0.23, the rate similarly decreases. This can be understood as at lower Ni(OH)₂ concentrations, not enough Ni(OH)₂ active sites are present on the surface of CdS. While at higher concentrations of Ni(OH)₂, the co-catalyst growth can occur quicker and thus, the photocatalytic rate is similar to the photocatalytic rate at longer reaction times: there is too much Ni(OH)₂ decoration which hinders photocatalysis. As this trend remains consistent for M(OH)_x (M = Co²⁺ and Fe³⁺), a similar conclusion can be made, too much M(OH)_x decoration and the co-catalyst partially blocks incident light Mn:CdS, too little M(OH)_x decoration and there are not enough active sites for photocatalysis.

Conclusions

To overcome the limitation of fast charge recombination of pristine CdS nanomaterials, we have developed noble metal free co-catalyst M(OH)_x (M = Ni²⁺, Co²⁺, and Fe³⁺) decorated Mn(II) doped 1D CdS NRs (*i.e.*, Mn:CdS-Ni(OH)₂ NRs) for photocatalytic hydrogen generation from water splitting. This is the first report of Mn(II) dopants utilized as charge transport bridges in non-noble metal co-catalysts for CdS-based photocatalysts. We also report the first use of Fe(OH)₃ as a co-catalyst for CdS. The energy transfer from 1D CdS host NRs to a long lifetime bridging Mn²⁺ ions followed by electron transfer to the self-regulating M(OH)_x/M(0) redox couple on the surface of the Mn:CdS-M(OH)_x NRs limits fast charge recombination in the host CdS NRs. Crucially, during photocatalysis, Ni(OH)₂ has the highest performance at neutral (pH = 7) while Co(OH)₂, and Fe(OH)₃ had the highest rate of photocatalysis at higher pH values (> 13). While neutral pH operation is desirable for practical water-splitting systems, the results presented here provide fundamental insights into charge-transfer processes and design principles for noble-metal-free co-catalysts. The higher rates of photocatalysis can be explained by a change in the thermodynamically stable phase of the metal hydroxide as revealed by Pourbaix diagram(s). Significant enhancement of the photocatalytic hydrogen generation rates came from the addition of Mn(II) dopants with noble metal free M(OH)_x co-catalyst islands to the CdS NRs of 109.2 times (112.0 mmol/g/h), 7.3 times (59.5 mmol/g/h), and 6.8 times (56.1 mmol/g/h), for Mn:CdS-Ni(OH)₂, Mn:CdS-Co(OH)₂, and Mn:CdS-Fe(OH)₃, respectively. Introducing noble metal free co-catalysts can provide new opportunities for both efficient charge separation



ARTICLE

Journal Name

and active sites in high performance photocatalysts for wide range industry applications.

Author contributions

Corresponding Author

*Xia Hu - School of Life and Environmental Sciences, Shaoxing University, Shaoxing, 312000, P. R. China; E-mail: huxia1111@usx.edu.cn

*Weiwei Zheng - Department of Chemistry, Syracuse University, Syracuse, New York 13244, United States; <http://orcid.org/0000-0003-1394-1806>; Email: wzhen104@syr.edu

Conflicts of interest

There are no conflicts to declare.

Acknowledgment

The research is sponsored by the Department of Chemistry and the Center of Excellence in Environmental and Energy Systems at Syracuse University.

Data availability

A data availability statement (DAS) is required to be submitted alongside all articles. Please read our [full guidance on data availability statements](#) for more details and examples of suitable statements you can use.

References

1. Lv, H.; Ruberu, T. P. A.; Fleischauer, V. E.; Brennessel, W. W.; Neidig, M. L.; Eisenberg, R. Catalytic Light-Driven Generation of Hydrogen from Water by Iron Dithiolene Complexes. *Journal of the American Chemical Society* **2016**, 138, (36), 11654-11663.
2. Xu, L.; Chen, M.; Hou, P.; Hou, X.; Wang, J.; Qi, Q.; Zhu, Y.; Yang, X.; Liu, X.; Li, X.; Jia, G.; Zhang, S.; Du, J. Synthesis of CdSe Nanowires and CulnSe₂ Nanosheets for Hydrogen Evolution. *ACS Appl. Nano Mater.* **2022**, 5, (2), 1935-1943.
3. Kim, W. D.; Kim, J.-H.; Lee, S.; Lee, S.; Woo, J. Y.; Lee, K.; Chae, W.-S.; Jeong, S.; Bae, W. K.; McGuire, J. A.; Moon, J. H.; Jeong, M. S.; Lee, D. C. Role of Surface States in Photocatalysis: Study of Chlorine-Passivated CdSe Nanocrystals for Photocatalytic Hydrogen Generation. *Chem. Mater.* **2016**, 28, (3), 962-968.
4. Fatahi, P.; Roy, A.; Bahrami, M.; Hoseini, S. J. Visible-Light-Driven Efficient Hydrogen Production from CdS NanoRods Anchored with Co-catalysts Based on Transition Metal Alloy Nanosheets of NiPd, NiZn, and NiPdZn. *ACS Appl. Energy Mater.* **2018**, 1, (10), 5318-5327.
5. Yang, W.; Peng, Q.; Yang, H.; Li, X.; Cao, J.; Wang, J.; Zheng, Y.; Li, C.; Pan, J. Hollow Co₃O₄/CdS Nanoparticles for Photocatalytic Hydrogen Evolution and Photodegradation. *ACS Appl. Nano Mater.* **2023**.
6. MacSwain, W.; Ma, D.-K.; Li, Z.-J.; Lin, H.; Bai, Y.-L.; Hu, X.; Zheng, W. Metal-based co-catalysts in semiconductor CdS hybrid nanostructures for enhanced photocatalysis: material design, mechanisms, and emerging trends. *Coord. Chem. Rev.* **2026**, 549, 217247.
7. Yu, J.; Yu, Y.; Zhou, P.; Xiao, W.; Cheng, B. Morphology-dependent photocatalytic H₂-production activity of CdS. *Appl. Catal., B* **2014**, 156-157, 184-191.
8. Yuan, J.; Wen, J.; Gao, Q.; Chen, S.; Li, J.; Li, X.; Fang, Y. Amorphous Co₃O₄ modified CdS nanorods with enhanced visible-light photocatalytic H₂-production activity. *Dalton Trans.* **2015**, 44, (4), 1680-1689.
9. Nasir, J. A.; Rehman, Z. U.; Shah, S. N. A.; Khan, A.; Butler, I. S.; Catlow, C. R. A. Recent developments and perspectives in CdS-based photocatalysts for water splitting. *J. Mater. Chem. A* **2020**, 8, (40), 20752-20780.
10. Jang, J. S.; Joshi, U. A.; Lee, J. S. Solvothermal Synthesis of CdS Nanowires for Photocatalytic Hydrogen and Electricity Production. *J. Phys. Chem. C* **2007**, 111, (35), 13280-13287.
11. Li, Q.; Zhao, F.; Qu, C.; Shang, Q.; Xu, Z.; Yu, L.; McBride, J. R.; Lian, T. Two-Dimensional Morphology Enhances Light-Driven H₂ Generation Efficiency in CdS Nanoplatelet-Pt Heterostructures. *Journal of the American Chemical Society* **2018**, 140, (37), 11726-11734.
12. MacSwain, W.; Lin, H.; Li, Z.-J.; Li, S.; Chu, C.; Dube, L.; Chen, O.; Leem, G.; Zheng, W. Facilitated electron transfer by Mn dopants in 1-dimensional CdS nanorods for enhanced photocatalytic hydrogen generation. *J. Mater. Chem. A* **2023**, 11, (13), 7066-7076.
13. Wu, K.; Chen, Z.; Lv, H.; Zhu, H.; Hill, C. L.; Lian, T. Hole removal rate limits photodriven H₂ generation efficiency in CdS-Pt and CdSe/CdS-Pt semiconductor nanorod-metal tip heterostructures. *J Am Chem Soc* **2014**, 136, (21), 7708-16.
14. Corby, S.; Rao, R. R.; Steier, L.; Durrant, J. R. The kinetics of metal oxide photoanodes from charge generation to catalysis. *Nat. Rev. Mater.* **2021**, 6, (12), 1136-1155.
15. Wang, J.; Xiong, L.; Bai, Y.; Chen, Z.; Zheng, Q.; Shi, Y.; Zhang, C.; Jiang, G.; Li, Z. Mn-Doped Perovskite Nanocrystals for Photocatalytic CO₂ Reduction: Insight into the Role of the Charge Carriers with Prolonged Lifetime. *Sol. RRL* **2022**, 6, (8), 2200294.
16. Zhu, Y.; Wang, Y.; Chen, Z.; Qin, L.; Yang, L.; Zhu, L.; Tang, P.; Gao, T.; Huang, Y.; Sha, Z.; Tang, G. Visible light induced photocatalysis on CdS quantum dots decorated TiO₂ nanotube arrays. *Appl. Catal. A Gen.* **2015**, 498, 159-166.
17. Rafiq, K.; Sabir, M.; Abid, M. Z.; Jalil, M.; Nadeem, M. A.; Iqbal, S.; Rauf, A.; Hussain, E. Tuning of TiO₂/CdS Hybrid Semiconductor with Au Cocatalysts: State-of-the-Art Design for Sunlight-Driven H₂ Generation from Water Splitting. *Energy Fuels* **2024**, 38, (5), 4625-4636.
18. Chen, Z.; Li, D.; Chen, C. Urchin-like TiO₂/CdS Nanoparticles Forming an S-scheme Heterojunction for Photocatalytic Hydrogen Production and CO₂ Reduction. *ACS Appl. Nano Mater.* **2023**, 6, (23), 21897-21908.
19. Wang, X.; Liu, G.; Wang, L.; Chen, Z. G.; Lu, G. Q.; Cheng, H. M. ZnO-CdS@Cd Heterostructure for Effective Photocatalytic Hydrogen Generation. *Adv. Energy Mater.* **2012**, 2, (1), 42-46.
20. Ma, D.; Wang, Z.; Shi, J.-W.; Zou, Y.; Lv, Y.; Ji, X.; Li, Z.; Cheng, Y.; Wang, L. An ultrathin Al₂O₃ bridging layer between CdS and ZnO



Journal Name

ARTICLE

boosts photocatalytic hydrogen production. *J. Mater. Chem. A* **2020**, 8, (21), 11031-11042.

21. Kim, Y. G.; Jo, W.-K. Photodeposited-metal/CdS/ZnO heterostructures for solar photocatalytic hydrogen production under different conditions. *Int. J. Hydrogen Energy* **2017**, 42, (16), 11356-11363.

22. Sultana, S.; Mansingh, S.; Scurrell, M.; Parida, K. M. Controlled Synthesis of CeO₂NS-Au-CdSQDs Ternary Nanoheterostructure: A Promising Visible Light Responsive Photocatalyst for H₂ Evolution. *Inorganic Chemistry* **2017**, 56, (20), 12297-12307.

23. Ijaz, S.; Ehsan, M. F.; Ashiq, M. N.; Karamat, N.; He, T. Preparation of CdS@CeO₂ core/shell composite for photocatalytic reduction of CO₂ under visible-light irradiation. *Appl. Surf. Sci.* **2016**, 390, 550-559.

24. Wu, K.; Chen, Z.; Lv, H.; Zhu, H.; Hill, C. L.; Lian, T. Hole Removal Rate Limits Photodriven H₂ Generation Efficiency in CdS-Pt and CdSe/CdS-Pt Semiconductor Nanorod-Metal Tip Heterostructures. *Journal of the American Chemical Society* **2014**, 136, (21), 7708-7716.

25. Daskalaki, V. M.; Antoniadou, M.; Li Puma, G.; Kondarides, D. I.; Lianos, P. Solar Light-Responsive Pt/CdS/TiO₂ Photocatalysts for Hydrogen Production and Simultaneous Degradation of Inorganic or Organic Sacrificial Agents in Wastewater. *Environ. Sci. Technol.* **2010**, 44, (19), 7200-7205.

26. Li, J.; Cushing, S. K.; Zheng, P.; Senty, T.; Meng, F.; Bristow, A. D.; Manivannan, A.; Wu, N. Solar Hydrogen Generation by a CdS-Au-TiO₂ Sandwich Nanorod Array Enhanced with Au Nanoparticle as Electron Relay and Plasmonic Photosensitizer. *Journal of the American Chemical Society* **2014**, 136, (23), 8438-8449.

27. Naya, S.-I.; Kume, T.; Akashi, R.; Fujishima, M.; Tada, H. Red-Light-Driven Water Splitting by Au(Core)-CdS(Shell) Half-Cut Nanoegg with Heteroepitaxial Junction. *Journal of the American Chemical Society* **2018**, 140, (4), 1251-1254.

28. Chava, R. K.; Im, Y.; Kang, M. Internal electric field promoted charge separation via bismuth-based ternary heterojunctions with near-infrared light harvesting properties for efficient photoredox reactions. *J. Mater. Chem. A* **2024**, 12, (29), 18498-18511.

29. Chava, R. K.; Kim, T.; Kim, Y.; Kang, M. Vanadium tetrasulfide as an earth-abundant and noble-metal-free cocatalyst for a solar-to-hydrogen conversion reaction. *J. Mater. Chem. C* **2023**, 11, (5), 1782-1790.

30. Chava, R. K.; Son, N.; Kang, M. Controllable oxygen doping and sulfur vacancies in one dimensional CdS nanorods for boosted hydrogen evolution reaction. *J. Alloys Compd.* **2021**, 873, 159797.

31. Chava, R. K.; Do, J. Y.; Kang, M. Enhanced photoexcited carrier separation in CdS-SnS₂ heteronanostructures: a new 1D-0D visible-light photocatalytic system for the hydrogen evolution reaction. *J. Mater. Chem. A* **2019**, 7, (22), 13614-13628.

32. Chen, Y.; Zhong, W.; Chen, F.; Wang, P.; Fan, J.; Yu, H. Photoinduced self-stability mechanism of CdS photocatalyst: The dependence of photocorrosion and H₂-evolution performance. *J. Mater. Sci. Technol.* **2022**, 121, 19-27.

33. Liu, Y.; Ding, S.; Shi, Y.; Liu, X.; Wu, Z.; Jiang, Q.; Zhou, T.; Liu, N.; Hu, J. Construction of CdS/CoO_x core-shell nanorods for efficient photocatalytic H₂ evolution. *Appl. Catal., B* **2018**, 234, 109-116.

34. Ning, X.; Li, J.; Yang, B.; Zhen, W.; Li, Z.; Tian, B.; Lu, G. Inhibition of photocorrosion of CdS via assembling with thin film TiO₂ and removing formed oxygen by artificial gill for visible light overall water splitting. *Appl. Catal., B* **2017**, 212, 129-139.

35. Kumar, V.; Singh, N.; Jana, S.; Rout, S. K.; Dey, R. K.; Singh, G. P. Surface polar charge induced Ni loaded CdS heterostructure nanorod for efficient photo-catalytic hydrogen evolution. *Int. J. Hydrogen Energy* **2021**, 46, (30), 16373-16386.

36. Zhang, L.; Zhu, X.; Zhao, Y.; Zhang, P.; Chen, J.; Jiang, J.; Xie, T. The photogenerated charge characteristics in Ni@NiO/CdS hybrids for increased photocatalytic H₂ generation. *RSC Adv.* **2019**, 9, (68), 39604-39610.

37. Ran, J.; Yu, J.; Jaroniec, M. Ni(OH)₂ modified CdS nanorods for highly efficient visible-light-driven photocatalytic H₂ generation. *Green Chem.* **2011**, 13, (10), 2708.

38. Lin, Y.-Z.; Wang, K.; Zhang, Y.; Dou, Y.-C.; Yang, Y.-J.; Xu, M.-L.; Wang, Y.; Liu, F.-T.; Li, K. Metal-organic framework-derived CdS-NiO heterostructures with modulated morphology and enhanced photocatalytic hydrogen evolution activity in pure water. *J. Mater. Chem. C* **2020**, 8, (29), 10071-10077.

39. Chen, X.; Chen, W.; Gao, H.; Yang, Y.; Shangguan, W. In situ photodeposition of NiO_x on CdS for hydrogen production under visible light: Enhanced activity by controlling solution environment. *Appl. Catal., B* **2014**, 152-153, 68-72.

40. Li, J.; Qian, X.; Peng, Y.; Lin, J. Hierarchical structure NiO/CdS for highly performance H₂ evolution. *Mater. Lett.* **2018**, 224, 82-85.

41. Khan, Z.; Khannam, M.; Vinothkumar, N.; De, M.; Qureshi, M. Hierarchical 3D NiO-CdS heteroarchitecture for efficient visible light photocatalytic hydrogen generation. *J. Mater. Chem.* **2012**, 22, (24), 12090.

42. Qiao, S.; Feng, C.; Guo, Y.; Chen, T.; Akram, N.; Zhang, Y.; Wang, W.; Yue, F.; Wang, J. CdS nanoparticles modified Ni@NiO spheres as photocatalyst for oxygen production in water oxidation system and hydrogen production in water reduction system. *Chem. Eng. J.* **2020**, 395, 125068.

43. Wang, L.; Wei, H.; Fan, Y.; Gu, X.; Zhan, J. One-Dimensional CdS/α-Fe₂O₃ and CdS/Fe₃O₄ Heterostructures: Epitaxial and Nonepitaxial Growth and Photocatalytic Activity. *J. Phys. Chem. C* **2009**, 113, (32), 14119-14125.

44. Yan, Z.; Yu, X.; Han, A.; Xu, P.; Du, P. Noble-Metal-Free Ni(OH)₂-Modified CdS/Reduced Graphene Oxide Nanocomposite with Enhanced Photocatalytic Activity for Hydrogen Production under Visible Light Irradiation. *J. Phys. Chem. C* **2014**, 118, (40), 22896-22903.

45. Lee, H.; Reddy, D. A.; Kim, Y.; Chun, S. Y.; Ma, R.; Kumar, D. P.; Song, J. K.; Kim, T. K. Drastic Improvement of 1D-CdS Solar-Driven Photocatalytic Hydrogen Evolution Rate by Integrating with NiFe Layered Double Hydroxide Nanosheets Synthesized by Liquid-Phase Pulsed-Laser Ablation. *ACS Sustain. Chem. Eng.* **2018**, 6, (12), 16734-16743.

46. Mao, L.; Ba, Q.; Liu, S.; Jia, X.; Liu, H.; Chen, W.; Li, X. Pt-Ni_x alloy nanoparticles: a new strategy for cocatalyst design on a CdS surface for photo-catalytic hydrogen generation. *RSC Adv.* **2018**, 8, (55), 31529-31537.

47. Xie, L.; Hao, J.-G.; Chen, H.-Q.; Li, Z.-X.; Ge, S.-Y.; Mi, Y.; Yang, K.; Lu, K.-Q. Recent advances of nickel hydroxide-based cocatalysts in heterogeneous photocatalysis. *Catal. Commun.* **2022**, 162, 106371.

48. Zhang, Y.; Wang, J.; Xu, N.; Wang, X.; Su, W. Ni(OH)₂ modified Mn_{0.5}Cd_{0.5}S with efficient photocatalytic H₂ evolution activity under visible-light. *Int. J. Hydrogen Energy* **2020**, 45, (41), 21532-21539.

49. Li, M.; Chen, F.; Xu, Y.; Tian, M. Ni(OH)₂ Nanosheet as an Efficient Cocatalyst for Improved Photocatalytic Hydrogen Evolution over Cd_{0.9}Zn_{0.1}S Nanorods under Visible Light. *Langmuir* **2024**, 40, (7), 3793-3803.

50. Wang, X.; Zhang, X.; Gao, W.; Sang, Y.; Wang, Y.; Liu, H. Self-reduction derived nickel nanoparticles in CdS/Ni(OH)₂ heterostructure for enhanced photocatalytic hydrogen evolution. *J. Chem. Phys.* **2020**, 152, (21), 214701.

51. Zhang, H.; Kong, X.; Yu, F.; Wang, Y.; Liu, C.; Yin, L.; Huang, J.; Feng, Q. Ni(OH)₂ Nanosheets Modified Hexagonal Pyramid CdS Formed



ARTICLE

Journal Name

Type II Heterojunction Photocatalyst with High-Visible-Light H₂ Evolution. *ACS Appl. Energy Mater.* **2021**, *4*, (11), 13152-13160.

52. Zhou, X.; Jin, J.; Zhu, X.; Huang, J.; Yu, J.; Wong, W.-Y.; Wong, W.-K. New Co(OH)₂/CdS nanowires for efficient visible light photocatalytic hydrogen production. *J. Mater. Chem. A* **2016**, *4*, (14), 5282-5287.

53. Xu, Y.; Xie, Z.; Yu, R.; Chen, M.; Jiang, D. Co(OH)₂ water oxidation cocatalyst-decorated CdS nanowires for enhanced photocatalytic CO₂ reduction performance. *Dalton Trans.* **2021**, *50*, (29), 10159-10167.

54. Ran, J.; Yu, J.; Jaroniec, M. Ni(OH)₂ modified CdS nanorods for highly efficient visible-light-driven photocatalytic H₂ generation. *Green Chem.* **2011**, *13*, (10), 2708-2713.

55. Yan, Z.; Yu, X.; Zhang, Y.; Jia, H.; Sun, Z.; Du, P. Enhanced visible light-driven hydrogen production from water by a noble-metal-free system containing organic dye-sensitized titanium dioxide loaded with nickel hydroxide as the cocatalyst. *Appl. Catal., B* **2014**, *160*-161, 173-178.

56. Lang, D.; Cheng, F.; Xiang, Q. Enhancement of photocatalytic H₂ production activity of CdS nanorods by cobalt-based cocatalyst modification. *Catal. Sci. Technol.* **2016**, *6*, (16), 6207-6216.

57. Wang, J.; Li, Y.; Shen, Q.; Izuishi, T.; Pan, Z.; Zhao, K.; Zhong, X. Mn doped quantum dot sensitized solar cells with power conversion efficiency exceeding 9%. *J. Mater. Chem. A* **2016**, *4*, (3), 877-886.

58. Dong, Y.; Choi, J.; Jeong, H.-K.; Son, D. H. Hot Electrons Generated from Doped Quantum Dots via Upconversion of Excitons to Hot Charge Carriers for Enhanced Photocatalysis. *Journal of the American Chemical Society* **2015**, *137*, (16), 5549-5554.

59. Dong, Y.; Parobek, D.; Rossi, D.; Son, D. H. Photoemission of Energetic Hot Electrons Produced via Up-Conversion in Doped Quantum Dots. *Nano Lett.* **2016**, *16*, (11), 7270-7275.

60. Li, W.; Ma, D.-K.; Hu, X.; Gou, F.; Yang, X.; MacSwain, W.; Qi, C.; Zheng, W. General strategy for enhanced CH₄ selectivity in photocatalytic CO₂ reduction reactions by surface oxophilicity engineering. *J. Catal.* **2022**, *415*, 77-86.

61. Jo, D.-Y.; Kim, D.; Kim, J.-H.; Chae, H.; Seo, H. J.; Do, Y. R.; Yang, H. Tunable White Fluorescent Copper Gallium Sulfide Quantum Dots Enabled by Mn Doping. *ACS Appl. Mater. Interfaces* **2016**, *8*, (19), 12291-12297.

62. Maity, P.; Kumar, R.; Jha, S. N.; Bhattacharyya, D.; Singh, R. K.; Chatterjee, S.; Ghosh, A. K. Unraveling the physical properties of Mn-doped CdS diluted magnetic semiconductor quantum dots for potential application in quantum spintronics. *J. Mater. Sci.: Mater. Electron.* **2022**, *33*, (27), 21822-21837.

63. Zheng, W.; Wang, Z.; Wright, J.; Goundie, B.; Dalal, N. S.; Meulenberg, R. W.; Strouse, G. F. Probing the Local Site Environments in Mn:CdSe Quantum Dots. *J. Phys. Chem. C* **2011**, *115*, (47), 23305-23314.

64. Liu, M.; Du, Y.; Ma, L.; Jing, D.; Guo, L. Manganese doped cadmium sulfide nanocrystal for hydrogen production from water under visible light. *Int. J. Hydrogen Energy* **2012**, *37*, (1), 730-736.

65. Pan, Z.; Wang, S.; Yan, R.; Song, C.; Jin, Y.; Huang, G.; Huang, J. Enhanced photocatalytic properties of Mn doped CdS catalysts by decomposition of complex precursors. *Opt. Mater.* **2020**, *109*, 110324.

66. Chen, H.-Y.; Maiti, S.; Son, D. H. Doping Location-Dependent Energy Transfer Dynamics in Mn-Doped CdS/ZnS Nanocrystals. *ACS Nano* **2012**, *6*, (1), 583-591.

67. Li, Z.-J.; Hofman, E.; Blaker, A.; Davis, A. H.; Dzikovski, B.; Ma, D.-K.; Zheng, W. Interface Engineering of Mn-Doped ZnSe-Based Core/Shell Nanowires for Tunable Host–Dopant Coupling. *ACS Nano* **2017**, *11*, (12), 12591-12600.

68. Li, S.; Lin, H.; Chu, C.; Martin, C.; MacSwain, W.; Meulenberg, R. W.; Franck, J. M.; Chakraborty, A.; Zheng, W. View Article Online Interfacial Site Selection Diffusion in All-Inorganic Core/Shell Perovskite Nanocrystals. *ACS Nano* **2023**, *17*, (22), 22467-22477.

69. Davis, A. H.; Hofman, E.; Chen, K.; Li, Z.-J.; Khammang, A.; Zamani, H.; Franck, J. M.; Maye, M. M.; Meulenberg, R. W.; Zheng, W. Exciton Energy Shifts and Tunable Dopant Emission in Manganese-Doped Two-Dimensional CdS/ZnS Core/Shell Nanoplatelets. *Chem. Mater.* **2019**, *31*, (7), 2516-2523.

70. Li, Z.-J.; Hofman, E.; Davis, A. H.; Khammang, A.; Wright, J. T.; Dzikovski, B.; Meulenberg, R. W.; Zheng, W. Complete Dopant Substitution by Spinodal Decomposition in Mn-Doped Two-Dimensional CsPbCl₃ Nanoplatelets. *Chem. Mater.* **2018**, *30*, (18), 6400-6409.

71. Li, Z.-J.; Li, S.; Davis, A. H.; Hofman, E.; Leem, G.; Zheng, W. Enhanced singlet oxygen generation by hybrid Mn-doped nanocomposites for selective photo-oxidation of benzylic alcohols. *Nano Res.* **2020**, *13*, (6), 1668-1676.

72. Saunders, A. E.; Ghezelbash, A.; Sood, P.; Korgel, B. A. Synthesis of High Aspect Ratio Quantum-Size CdS Nanorods and Their Surface-Dependent Photoluminescence. *Langmuir* **2008**, *24*, (16), 9043-9049.

73. Chen, J. S.; Zhu, T.; Hu, Q. H.; Gao, J.; Su, F.; Qiao, S. Z.; Lou, X. W. Shape-Controlled Synthesis of Cobalt-based Nanocubes, Nanodiscs, and Nanoflowers and Their Comparative Lithium-Storage Properties. *ACS Appl. Mater. Interfaces* **2010**, *2*, (12), 3628-3635.

74. Zhang, L. J.; Zheng, R.; Li, S.; Liu, B. K.; Wang, D. J.; Wang, L. L.; Xie, T. F. Enhanced Photocatalytic H₂ Generation on Cadmium Sulfide Nanorods with Cobalt Hydroxide as Cocatalyst and Insights into Their Photogenerated Charge Transfer Properties. *ACS Appl. Mater. Interfaces* **2014**, *6*, (16), 13406-13412.

75. Zhao, Z.; Zhang, H.; Chen, P.; Jin, G.; Wu, L. Fe(OH)₃/Ti₃C₂T_x nanocomposites for enhanced ammonia gas sensor at room temperature. *Nanotechnology* **2024**, *35*, (50), 505502.

76. Nagaraju, G.; Ko, Y. H.; Yu, J. S. Self-assembled hierarchical β -cobalt hydroxide nanostructures on conductive textiles by one-step electrochemical deposition. *CrystEngComm* **2014**, *16*, (48), 11027-11034.

77. Yost, A. J.; Ekanayaka, T. K.; Gurung, G.; Rimal, G.; Horoz, S.; Tang, J.; Paudel, T.; Chien, T. Influence of the Cation on the Surface Electronic Band Structure and Magnetic Properties of Mn:ZnS and Mn:CdS Quantum Dot Thin Films. *J. Phys. Chem. C* **2019**, *123*, (40), 24890-24898.

78. Zhao, J.; Lu, Z.; He, X.; Zhang, X.; Li, Q.; Xia, T.; Zhang, W.; Lu, C. Fabrication and Characterization of Highly Porous Fe(OH)₃@Cellulose Hybrid Fibers for Effective Removal of Congo Red from Contaminated Water. *ACS Sustain. Chem. Eng.* **2017**, *5*, (9), 7723-7732.

79. Abdelmoula, M.; Ruby, C.; Mallet, M.; Ghanbaja, J.; Coustel, R.; Scudiero, L.; Wang, W.-J. Identification of a Fe(OH)₂-like phase in the core–shell structure of nano-zero-valent Fe and its evolution when interacting with Pd^{2+aq} ions by Mössbauer spectroscopy, XPS, and TEM. *J. Phys. Chem. Solids* **2023**, *172*, 111066.

80. Wang, L.; Zhang, H.; Li, Y.; Xiao, S.; Bi, F.; Zhao, L.; Gai, G.; Yang, X. Construction of bundle-like cobalt/nickel hydroxide nanorods from metal organic framework for high-performance supercapacitors. *J. Mater. Sci.: Mater. Electron.* **2022**, *33*, (13), 10540-10550.

81. Li, X.; Patil, K.; Agarwal, A.; Babar, P.; Jang, J. S.; Chen, X.; Yoo, Y. T.; Kim, J. H. Ni(OH)₂ Coated CoMn-layered double hydroxide nanowires as efficient water oxidation electrocatalysts. *New J. Chem.* **2022**, *46*, (5), 2044-2052.



Journal Name

ARTICLE

82. Kudielka, A.; Schmid, M.; Klein, B. P.; Pietzonka, C.; Gottfried, J. M.; Harbrecht, B. Nanocrystalline cobalt hydroxide oxide: Synthesis and characterization with SQUID, XPS, and NEXAFS. *J. Alloys Compd.* **2020**, *824*, 153925.

83. Hofman, E.; Robinson, R. J.; Li, Z.-J.; Dzikovski, B.; Zheng, W. Controlled Dopant Migration in CdS/ZnS Core/Shell Quantum Dots. *J Am Chem Soc* **2017**, *139*, (26), 8878-8885.

84. Chu, C.; Hofman, E.; Gao, C.; Li, S.; Lin, H.; MacSwain, W.; Franck, J. M.; Meulenberg, R. W.; Chakraborty, A.; Zheng, W. Inserting an "atomic trap" for directional dopant migration in core/multi-shell quantum dots. *Chem. Sci.* **2023**, *14*, (48), 14115-14123.

85. Hofman, E.; Khammang, A.; Wright, J. T.; Li, Z.-J.; McLaughlin, P. F.; Davis, A. H.; Franck, J. M.; Chakraborty, A.; Meulenberg, R. W.; Zheng, W. Decoupling and Coupling of the Host–Dopant Interaction by Manipulating Dopant Movement in Core/Shell Quantum Dots. *J. Phys. Chem. Lett.* **2020**, *11*, (15), 5992-5999.

86. He, W.; Li, X.; An, S.; Li, T.; Zhang, Y.; Cui, J. 3D β -Ni(OH)₂ nanowires/RGO composite prepared by phase transformation method for superior electrochemical performance. *Sci. Rep.* **2019**, *9*, (1), 10838.

87. Trafela, Š.; Zavašnik, J.; Šturm, S.; Rožman, K. Ž. Formation of a Ni(OH)₂/NiOOH active redox couple on nickel nanowires for formaldehyde detection in alkaline media. *Electrochim. Acta* **2019**, *309*, 346-353.

88. Xie, R.-C.; Batchelor-McAuley, C.; Rauwel, E.; Rauwel, P.; Compton, R. G. Electrochemical Characterisation of Co@Co(OH)₂ Core-Shell Nanoparticles and their Aggregation in Solution. *ChemElectroChem* **2020**, *7*, (20), 4259-4268.

89. Duschek, K.; Uhlemann, M.; Schlörb, H.; Nielsch, K.; Leistner, K. Electrochemical and *in situ* magnetic study of iron/iron oxide films oxidized and reduced in KOH solution for magneto-ionic switching. *Electrochim. Commun.* **2016**, *72*, 153-156.

90. Belson, H. S. Shiftless Fermi Level in Iron, Nickel, and Cobalt. *J. Appl. Phys.* **1966**, *37*, (3), 1348-1349.

91. Scanlon, M. D.; Peljo, P.; Méndez, M. A.; Smirnov, E.; Girault, H. H. Charging and discharging at the nanoscale: Fermi level equilibration of metallic nanoparticles. *Chem. Sci.* **2015**, *6*, (5), 2705-2720.

92. Reiss, H. The Fermi level and the redox potential. *J. Phys. Chem.* **1985**, *89*, (18), 3783-3791.

93. Mishra, B. P.; Dahiya, J.; Krishnan, V. Semiconductor photocatalysts for hydrogen evolution: critical role of cocatalysts in enhancing performance. *Chem. Commun.* **2025**, *61*, (89), 17302-17329.

94. Huang, L. F.; Hutchison, M. J.; Santucci, R. J., Jr.; Scully, J. R.; Rondinelli, J. M. Improved Electrochemical Phase Diagrams from Theory and Experiment: The Ni–Water System and Its Complex Compounds. *J. Phys. Chem. C* **2017**, *121*, (18), 9782-9789.

95. Pourbaix, M. J. N. In *Atlas of Electrochemical Equilibria in Aqueous Solutions*, 1974.

96. Okumusoglu, D.; Gündüz, O. Hydrochemical Status of an Acidic Mining Lake in Çanakkale, Turkey. *Water Environment Research* **2013**, *85*, (7), 604-620.

97. Chivot, J.; Mendoza, L.; Mansour, C.; Pauporté, T.; Cassir, M. New insight in the behaviour of Co–H₂O system at 25–150°C, based on revised Pourbaix diagrams. *Corros. Sci.* **2008**, *50*, (1), 62-69.

98. Weinrich, H.; Durmus, Y. E.; Tempel, H.; Kungl, H.; Eichel, R.-A. Silicon and Iron as Resource-Efficient Anode Materials for Ambient-Temperature Metal-Air Batteries: A Review. *Materials* **2019**, *12*, (13), 2134.

99. Garcia, E. M.; Santos, J. S.; Pereira, E. C.; Freitas, M. B. J. G. Electrodeposition of cobalt from spent Li-ion battery cathodes by the electrochemistry quartz crystal microbalance technique. *J. Power Sources* **2008**, *185*, (1), 549-553. DOI: 10.1039/DSTA08886K

100. Li, Z.-J.; Wang, J.-J.; Li, X.-B.; Fan, X.-B.; Meng, Q.-Y.; Feng, K.; Chen, B.; Tung, C.-H.; Wu, L.-Z. An Exceptional Artificial Photocatalyst, Ni_h-CdSe/CdS Core/Shell Hybrid, Made *In Situ* from CdSe Quantum Dots and Nickel Salts for Efficient Hydrogen Evolution. *Adv. Mater.* **2013**, *25*, (45), 6613-6618.

101. Simon, T.; Bouchonville, N.; Berr, M. J.; Vaneski, A.; Adrović, A.; Volbers, D.; Wyrwich, R.; Döblinger, M.; Susha, A. S.; Rogach, A. L.; Jäckel, F.; Stolarszky, J. K.; Feldmann, J. Redox shuttle mechanism enhances photocatalytic H₂ generation on Ni-decorated CdS nanorods. *Nat. Mater.* **2014**, *13*, (11), 1013-1018.

102. Silva, L. A.; Ryu, S. Y.; Choi, J.; Choi, W.; Hoffmann, M. R. Photocatalytic Hydrogen Production with Visible Light over Pt-Interlinked Hybrid Composites of Cubic-Phase and Hexagonal-Phase CdS. *J. Phys. Chem. C* **2008**, *112*, (32), 12069-12073.

103. Wang, Z.; Meijerink, A. Concentration Quenching in Upconversion Nanocrystals. *J. Phys. Chem. C Nanomater Interfaces* **2018**, *122*, (45), 26298-26306.

104. Cao, J.; Yang, J.; Zhang, Y.; Yang, L.; Wang, Y.; Wei, M.; Liu, Y.; Gao, M.; Liu, X.; Xie, Z. Optimized doping concentration of manganese in zinc sulfide nanoparticles for yellow-orange light emission. *J. Alloys Compd.* **2009**, *486*, (1-2), 890-894.



Data Availability Statement

for

Noble-Metal-Free Metal Hydroxide Co-Catalyst Coupled Mn(II)-Doped CdS Nanorods with
Bridged Charge Transport for Enhanced Photocatalytic Hydrogen Generation

*Walker MacSwain,^b Xia Hu,^{†a} Rongzhen Wu,^c Zhi-Jun Li,^b Vanshika Vanshika,^b De-Kun Ma,^d Ou Chen,^c Weiwei
Zheng^{b†}*

The authors confirm that all data supporting the findings of this study are available
within the article and its supplementary materials.

